Interaction of Vortex Shedding Processes on Flow over a Deep-Draft Semi-Submersible

Yibo Liang, Longbin Tao*

School of Marine Science and Technology, Newcastle University, Newcastle upon Tyne, NE1 7RU, UK

Abstract

A numerical study on the flow over a Deep-Draft Semi-Submersible (DDS) for both stationary and Vortex-Induced Motions (VIM) was carried out using the Computational Fluid Dynamics (CFD), with the aim to investigate the overall hydrodynamics of the structure. In order to study the fluid physics associated with VIM, a comprehensive numerical simulation was conducted to examine the characteristics of vortex formations, shedding processes and especially their interactions due to the multiple cylindrical columns. In addition to the vortex shedding characteristics, the drag and lift forces on each member of the overall structure were calculated. It is revealed that under 45° incidence, the transverse forces induced by the portside and starboard side columns are the dominant excitation forces responsible to VIM while the horizontal member - pontoons restraining VIM. In addition, the hysteresis phenomenon observed between the force and motion domains - the peak lift force occurs slightly earlier than the peak transverse motion is mainly due to the vortices shed from the upstream column move back to impinge on one of the side columns after impinging on the other side column and the symmetrical strong vortices which shed from the side columns.

Keywords

* Corresponding author. Tel.: +44 (0) 191 208 6670; Fax: +44 (0) 191 208 5491; E-mail address: longbin.tao@newcastle.ac.uk

Vortex-Induced Motions (VIM); Deep-Draft Semi-Submersible (DDS); Computational Fluid Dynamics (CFD)

Nomenclature

A_x/L	Non-dimensional characteristics amplitude of in-line motion
A_y/L	Non-dimensional characteristics amplitude of transverse motion
B_L	Platform width
B_T	Platform draft
C_a	Added mass coefficient
C_D	Drag force coefficient
C_L	Lift force coefficient
D	Column projected length
f	Vortex shedding frequency
f_0	Natural frequency in still water
Fr	Froude number
F_D	Hydrodynamic drag force acting on the structure
F_L, F_y	Hydrodynamic lift force acting on the structure
GCI	Grid convergence index
H	Immersed column height above the pontoon
L	Column width
m	Platform mass
m_a	Added mass
P	Pontoon height
Re	Reynolds number
rms	Root mean square
S	Distance between centre columns
St	Strouhal number
T_0	Natural periods in still water
Δt	Numerical simulation time step
U, U_c	Current speed
Ur	Reduced velocity
ρ	Fresh water density

52	Δ	Displacement
53	λ	Scale ratio
54	$\vec{\omega}_x$	Streamwise vorticity
55	$\vec{\omega}_y$	Transverse vorticity
56	$\vec{\omega}_z$	Spanwise vorticity
57	X	In-line motion
58	Y	Transverse motion
59	y^+	Y plus value

60 1. Introduction

61 Vortex-Induced Motions (VIM) have been receiving continuous attention in the field of offshore
62 exploration and exploitation as an increasing number of deep-draft floating structures have been
63 operating in different regions around world. Deep-draft floating structures are well known for their
64 favourable vertical motions behaviour compared with other types of floating offshore structures.
65 However, the increases in the structure's draft can also lead to more severe VIM, which may lead to
66 potential damage particularly causing fatigue to the mooring and riser systems.

67 VIM have often been observed since the Genesis Spar platform was commissioned in 1997 (Fujarra et
68 al., 2012; Kokkinis et al., 2004). Rijken and Leverette (2009) reported VIM phenomenon on a semi-
69 submersible in field measurements. Ma et al. (2013) also observed the presence of VIM from recent
70 field measurements. In this aspect, a number of studies on the VIM behaviours have been carried out,
71 including both experimental and numerical studies. On the experimental investigation side, as pointed
72 out by Fujarra et al. (2012) in their comprehensive review, VIM are now much better understood.
73 However, it is still lack of understanding about the VIM mechanism on multiple cylindrical structures
74 such as the semi-submersible and the Tension-Leg Platform (TLP). The vortex shedding processes
75 and subsequent VIM are much more complex than those of single cylindrical structures due to the
76 multi-columns, pontoons and their interactions with the vortex shedding processes.

77 Waals et al. (2007) conducted several VIM tests on both DDS and TLP to examine the influences of
78 mass ratio and draft effects. A series of model tests on a DDS were carried out by Hong et al. (2008),

and the results showed that under a strong current, the DDS will have more significant VIM responses compared with the wave-current coupling condition. Rijken and Leverette (2008) experimentally studied the VIM responses of a DDS, and observed that wave and external damping can affect the VIM responses. Through their tests, it was noted that the relatively low sea states do not particularly influence the VIM responses under the so-called “lock-in” region. Moreover, the additional damping delayed the onset of VIM to a higher reduced velocity. Rijken et al. (2011) analysed the influences of SCR systems and appurtenances on VIM for a DDS. Their work showed that the appurtenances on the vertical faces of the columns and above the pontoon can alter the VIM responses. Gonçalves et al. (2012) subsequently investigated the effects of the current angle and appendages on a conventional semi-submersible. The presence of VIM on a conventional semi-submersible has been confirmed in their works. Following on from their initial outcomes, Gonçalves et al. (2013) further studied other relevant factors such as the draft conditions, the external damping and wave effects on VIM developing by performing a series of towing tank tests. Additionally, Gonçalves et al. (2015) performed experimental tests focusing on the effects of different column designs on the VIM responses. The results showed that the circle section shaped column design has the most severe transverse motions at 0 degree flow incidence and that the square section shaped column design has the most significant transverse motion at 45 degree flow incidence. Recently, Antony et al. (2016) studied the effects of damping on VIM and investigated the force distribution on each member of the structure in detail by an experimental routine. The work done by each member was presented in their investigations. The investigations showed that for 45 degree flow incidence, when the maximum transverse VIM response occurs, three upstream columns excited VIM. The horizontal member - pontoons, however, were noted to limit the VIM responses.

In the last decade, the continued technological advances offer ever-increasing computational power, in which CFD methods are rapidly gaining popularity for VIM predictions. Lefevre et al. (2013) proposed the guidelines for undertaking the Spar VIM simulations. Tan et al. (2013) performed a series of CFD simulations for VIM on a multi-column floater. Lee et al. (2014) studied the differences between the prototype and model VIM responses by numerical predictions. Antony et al. (2015)

numerically and experimentally investigated the VIM responses of a deep-draft column stabilized floater. Their work shows that the damping effects of the riser and mooring systems are very important in CFD simulations. Vinayan et al. (2015) increased the confidence for CFD simulations on the VIM predictions of a deep-draft column stabilized floater through a series of numerical simulations on a PC-semi with different drafts and arrangements. Liu et al. (2015) numerically investigated the effects of pontoon on hydrodynamic forces for a stationary DDS model and revealed that the DDS with the different numbers of pontoons affects both drag and lift forces on the stationary structures. Koop et al. (2016) carried out a series of CFD studies to illustrate the results of the scale and damping effects for VIM on a semi-submersible. Their work showed that the scale effects at 45 degree incidence are less than that at 0 degree incidence. Under 45 degree incidence, the VIM response at prototype Reynolds number is found to be similar compared with that at model scale Reynolds number. Similar observation was also reported by Lee et al. (2014).

2. Numerical simulation

2.1. Computational overview

A comprehensive numerical study was conducted in this section, with the aim to examine the vortex shedding characteristics and the associated fluid dynamics. The numerical schemes are introduced and followed by a sensitivity assessment in order to perform a computationally efficient numerical analysis.

The Detached Eddy Simulation (DES) method was used in this study. For the DES model, the Improved Delayed Detached Eddy Simulation (IDDES) model (Shur et al., 2008) with the Spalart-Almaras (SA) (Spalart et al., 1997) was used. All the simulations were carried out by using a Star-CCM+ 9 package.

The principle dimensions of the deep-draft semi-submersible analysed in this section are given in Table 1. Two models with different scale ratios are simulated in the present study, with resulting flow

conditions ranging from Reynolds number 3×10^5 to 1.1×10^6. Model I is used for the stationary structure simulations where the model scale ratio is 1:128. Model II is for the VIM simulations where the model scale ratio is 1:64. For all simulations, the computational domain $9B_L \times 6B_L \times 3B_T$ is used (where B_L is the overall hull width of the semi-submersible and B_T is the draft of the semi-submersible) based on the convergence study. The computational domain were $6B_L \times 4.5B_L \times 2.8B_T$ and $5B_L \times 4B_L \times 2.2B_T$ in the studies by Lee et al. (2014). Tan et al. (2013) performed their analysis using a $27B_L \times 18B_L \times 6.5B_T$ domain and Liu et al. (2015) used a $11B_L \times 6B_L \times 3B_T$ domain. Koop et al. (2016) chose a $10B_L \times 6B_T$ cylindrical domain. Compared with aforementioned computational domain sizes, a $9B_L \times 6B_L \times 3B_T$ domain (see Fig. 2) was considered to be large enough to eliminate the far field effects from the boundaries and the three-dimensional effects from a spanwise cross flow direction.

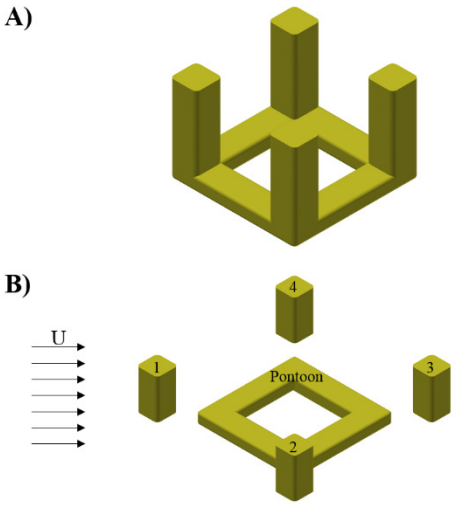

Fig. 1. The DDS model (A is the entire model and B is the decomposed model which show the definition of the individual members).

Table 1. Main characteristics of the DDS unit (The model I is the stationary model which presents scale ratio as 1:128, and the model II is the VIM model which presents scale ratio as 1:64).

	Prototype (m)	Model I (m)	Model II (m)
Distance between centre columns (S)	72.5	0.567	1.133
Column width (L)	19.5	0.152	0.305
Immersed column height above the pontoon (H)	37.0	0.289	0.578
Pontoon height (P)	10.0	0.078	0.156

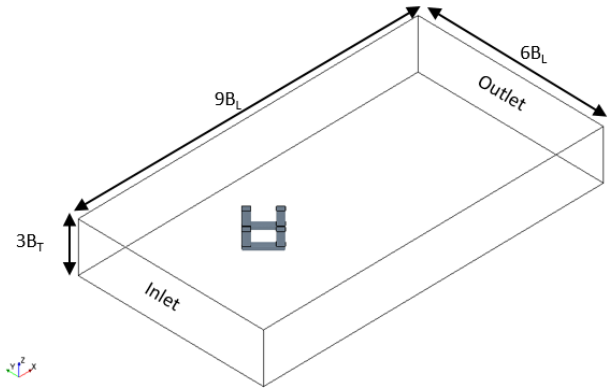

Fig. 2. Computational domain.

The polyhedral mesh (CD-adapco, 2014) was used in the present study. The overall elements mesh is shown at a middle-depth horizontal layer in Fig. 3. In the present study, a near wall refinement method named "Prism Layer Mesher" is adopted. The y^+ values are smaller than 1 in all simulations, where $y^+ = u_* \Delta y_1 / v$ (u_* denotes the friction velocity at the nearest wall, Δy_1 is the first layer thickness and v is the kinematic viscosity). Other five regional refinements are carried out in the domain to refine both the near wake and the far wake region (see Fig. 4).

The boundary conditions are kept all the same in the present study. At the inlet, a uniform and constant velocity is specified directly for all sensitivity studies. The pressure at boundary was extrapolated from the adjacent cell using reconstruction gradients (CD-adapco, 2014). Along the outlet boundary, the pressure is prescribed to be equal to zero. The velocity at the boundary was extrapolated from the interior using reconstruction gradients (CD-adapco, 2014). For the body surface of the deep-draft semi-submersible, a no-slip boundary condition was specified in terms of the tangential velocity which is explicitly set to be zero and the pressure at the boundary was extrapolated from the adjacent cells using reconstruction gradients (CD-adapco, 2014). As the Froude number is

quite small (Fr < 0.2) in all simulations, the free surface effects can be ignored and the free surface boundary condition is prescribed as being a symmetry boundary.

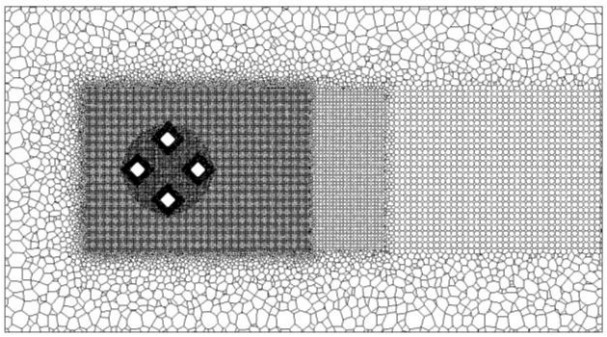

Fig. 3. Visualisation of the mesh at the middle draft level of the DDS (XY plane at the middle draft of the DDS).

2.2. Sensitivity studies

In order to investigate the numerical mesh sensitivity of the calculated results, a mesh sensitivity study had been carried out with different levels of refinement grids resolution following the guideline proposed by Celik et al. (2008). The Reynolds number set for the mesh sensitivity study is 1.1×10^6, which is the highest Reynolds number in all the undertaken simulations. The details of the mesh sensitivity studies are shown in Table 2. Results for all cases are obtained by averaging after more than fifteen vortex shedding cycles.

Table 2. Calculations of discretization error (Celik et al., 2008); GCI index represents the numerical uncertainty.

	$\overline{C}_D$	C_{Lrms}	St
N_1, N_2, N_3 **(thousand)**	6860, 3430, 937	6860, 3430, 937	6860, 3430, 937
r_{21}	1.333	1.333	1.333
r_{32}	1.6	1.6	1.6
$\emptyset_1$	1.066	0.093	0.131
$\emptyset_2$	1.068	0.101	0.131
$\emptyset_3$	1.053	0.139	0.134
p	4.561	2.961	NaN

GCI^{32}_{normal}	0.23%	18.31%	NaN
GCI^{21}_{fine}	0.09%	9.13%	NaN

Following the guideline proposed by Celik et al. (2008), N_3, N_2, N_1 represent the total number of grids from a course grid refinement level to a relatively fine grid refinement; r is the grid refinement factor, where $r = h_{coarse}/h_{fine}$ and h is the grid size; Ø is the calculation results for different grid refinements; p is the apparent order; GCI is the grid convergence index which shows the level of numerical uncertainty. The resulting force coefficients (C_D, C_L) and the Strouhal number (St) which are compared in the sensitivity studies are defined as:

$$C_D = \frac{F_D}{\frac{1}{2}\rho U_C^2 A}, \quad (1)$$

$$C_L = \frac{F_L}{\frac{1}{2}\rho U_C^2 A}, \quad (2)$$

$$St = \frac{fL}{U_c}, \quad (3)$$

where, F_D is the drag force on the structure, F_L is the lift force on the structure, ρ is the fresh water density, U_C is the free stream velocity, A is the projected area of the immersed structure, f is the vortex shedding frequency obtained from the power spectra of lift force coefficient fluctuations as followed by Schewe (1983) and L is the width of the DDS column.

As shown in Table 2, there is a reduction in the GCI index for the successive finer grid refinements, where GCI^{21}_{fine} is less than GCI^{32}_{normal}. The GCI index for the fine grid refinement (GCI^{21}_{fine}) is relatively low compared to the coarse level of grid refinement (GCI^{32}_{normal}), indicating that the dependence of the numerical simulation on the mesh has been reduced. As the GCI index reduction from the coarse grid refinement to the fine grid refinement is relatively high, then the mesh convergence (grid independent) can be said to have been nearly achieved. Additionally, as the St may indicate that the "exact" solution has been attained, in this case, calculations with additional grid refinements are

performed in Fig. 4. It shows that the *St* is converged around the value of 0.131. Therefore, the numerical uncertainty for the Strouhal number is shown as "NaN" in Table 2. These mesh sensitivity studies show that the N_2 numerical mesh setting is fine enough to obtain reliable results with an acceptable computation time and they are used in further numerical studies.

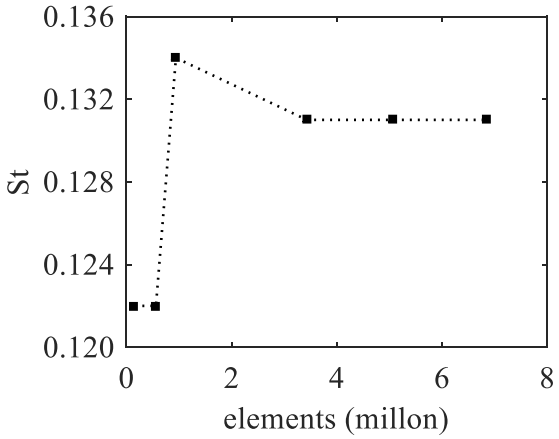

Fig. 4. Calculations with additional grid refinements for the Strouhal number (*St*).

The non-dimensional time step is chosen as 0.008 (non-dimensional time step = $\Delta tU/L$, where Δt is the time step, U is the inlet velocity and L is the width of the DDS column) for all cases based on sensitivity test. The constant non-dimensional time step size will result in varying courant (CFL) numbers as the grid is refined. A major benefit of employing the IDDES approach is that a large portion of the flow should be resolved with the Large Eddy Simulation (LES), but this requires rather strict CFL number limits. In the present study, the CFL numbers for the majority of the overall flow region are less than 1. Only in some tiny flow areas, the CFL numbers are found to be between 1 to 2. Therefore, the time step is considered to be fine enough for the current simulations' requirement (Liang et al., 2016).

2.3. Reduced velocity

When discussing VIM, the so-called reduced velocity (*Ur*) is usually used as the reference value. The reduced velocity (*Ur*) is defined as:

214 $$Ur = \frac{UT_0}{D}, \quad (4)$$

215 where U is the current speed, T_0 is the natural period of the motions in calm water and D is the
216 projected length of the column.

217 3. Results and discussion

218 Two different conditions (stationary and VIM) of a typical deep-draft semi-submersible under 45
219 degree flow incidence were investigated using the present numerical model and their results are
220 further compared with the experimental data from model tests conducted in a circulating water
221 channel and a towing tank respectively.

222 The results from both previous works and present outcomes are summarised in Table 3. As confirmed
223 in both field measurements and model tests (Gonçalves et al., 2012; Koop et al., 2016; Lee et al.,
224 2014; Ma et al., 2013; Magee et al., 2011; Rijken and Leverette, 2008; Waals et al., 2007), for square
225 section shaped multi-columns structures, the most severe transverse motion occurred at 45 degree
226 incidence. As Koop et al. (2016) noted, the scale effects of a DDS in a 45 degree flow are less than
227 that in a 0 degree flow. This indicates that the Reynolds number does not have a large effect on the
228 model predictions at 45 degree incidence. Aiming to investigate the VIM of a DDS at a realistic field
229 condition with the real engineering applications, the flow over a stationary structure and a VIM model
230 of a DDS at 45 degree incidence have been numerically investigated after a rigorous validation
231 against the experimental data. The hydrodynamic loads on different members of the structure, such as
232 four columns and pontoons, are compared in order to quantify the determining factors which induced
233 VIM excitation. Moreover, the flow patterns are further examined to reveal the insights of the vortex
234 dynamics associated with VIM.

235 Table 3. Summary of the various studies on VIM of the multiple square section shaped columns
236 structures.

	λ	H/L	Ur	max A_y/L at 0°	max A_y/L at 45°
Waals et al. (2007)	1:70	1.75	4.0~40.0	--	0.320
Rijken and Leverette (2008)	1:50	2.18	1.0~15.0	0.151	0.468
Magee et al. (2011)	1:70	1.50	4.0~13.0	0.269	0.319
Gonçalves et al. (2012)	1:100	1.14	2.5~20.0	0.268	0.382
Ma et al. (2013)	1:1	--	3.2~13.7	0.163	0.218
Lee et al. (2014)	1:67	1.78	4.0~20.0	--	0.393
Lee et al. (2014)	1:1	1.78	4.0~20.0	--	0.344
Koop et al. (2016)	1:54	--	3.0~10.0	--	0.470
Present work	1:64	1.90	3.4~14.1	0.279	0.742

3.1. *"lock-in"* phenomenon

The "lock-in" phenomenon is defined as being the synchronized oscillation region that is experienced as VIM develops. When flow over a bluff body, vortices are generated on the downstream area of the structure which are detached periodically and alternately from each opposite sides of the structure. The structure affected by the vortex shedding may thus begin oscillating either side to side or in a fore and aft manner. If the vortex shedding frequency closes to the natural frequency of the structure, the motion can be amplified. This amplification phenomenon is named as the "lock-in". The "lock-in" always happened at reduced velocity around seven (See Fig. 5). It can be clearly seen in Fig. 5 that the structure experiences the largest transverse motions at 45 degree incidence. Fig. 6 shows the spanwise vorticity contour ($\vec{\omega}_z D/U$) when the "lock-in" generated. Under 45 degree incidence, the non-dimensional spanwise vorticity is stronger than that under 0 degree incidence. In the present investigation, the hydrodynamic loads on the structures and the vortex shedding interactions under 45 degree incidence are analysed and discussed.

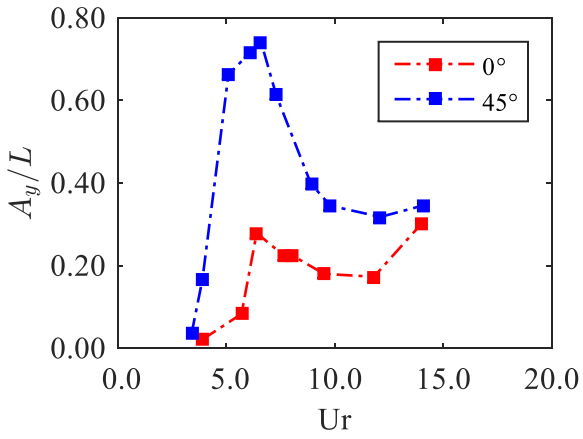

Fig. 5. Non-dimensional transverse characteristic amplitudes (A_y/L) obtained from the present towing tank test.

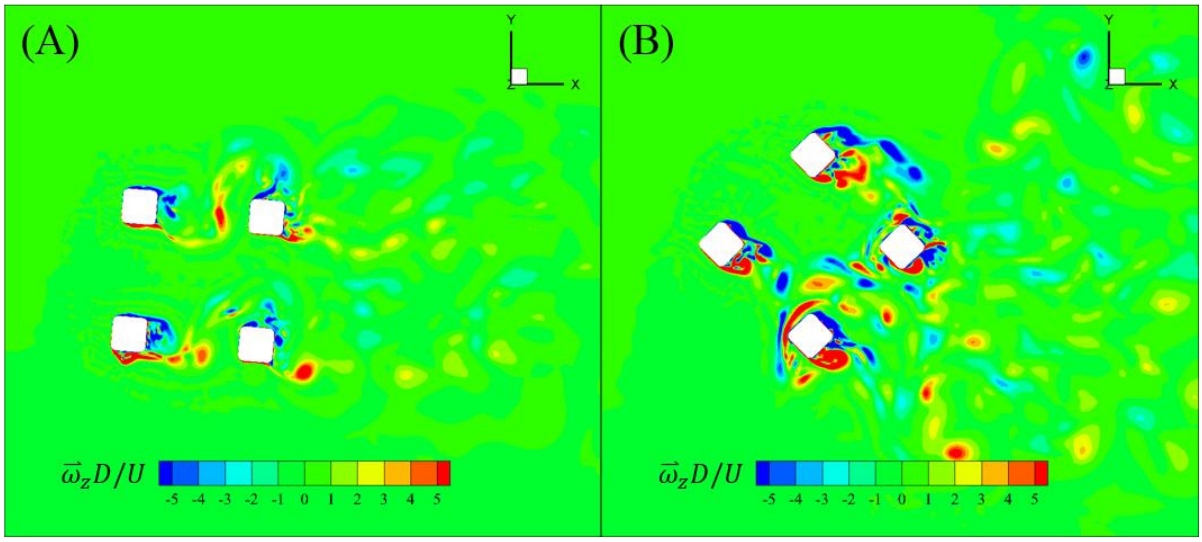

Fig. 6. Non-dimensional spanwise vorticity ($\vec{\omega}_z D/U$) contours around the DDS at middle draft showing the flow fields when "lock-in" has occurred (A: Ur = 6.4, 0 degree incidence. B: Ur = 6.6, 45 degree incidence).

3.2. Stationary model results and observations

In this section, a numerical study of the flow over a stationary deep-draft semi-submersible model with Reynolds numbers varying from 3.7×10^4 to 6.0×10^4 was carried out in order to investigate the

overall hydrodynamics. Results for all cases were obtained by averaging after more than fifteen vortex shedding cycles. These numerical predictions are subsequently validated by the force measurements from the corresponding experimental measurements which have been undertaken in a circulating water channel. The characteristics of vortex shedding processes and their interactions due to the multiple cylindrical column arrangement are examined in detail.

3.2.1. Overall drag and lift forces on the DDS

The overall fluid drag and lift forces are presented as the non-dimensional force coefficients C_D and C_L. Details of the numerical results are given in Table 4.

Table 4. The resulting force coefficient values $\overline{C}_D$, C_{Lrms} and St for the flow over a stationary DDS.

Re	$\overline{C}_D$	C_{Lrms}	St
3.7×10^4	1.068	0.070	0.140
4.3×10^4	1.046	0.069	0.138
5.2×10^4	1.044	0.066	0.143
6.0×10^4	1.053	0.080	0.142

These numerical results are validated by the force measurements obtained from the corresponding experimental data. The experiments were conducted in a circulating water channel. The circulating water channel is vertically oriented with an 8.0m length, 3.0m width and 1.6m depth measuring section. The range of the flow velocity is 0.1 ~ 3m/s, and the minimum fluctuations of the current velocity speed is 0.01m/s. The total fluid forces on the model I was measured by a three-component force transducer.

Comparisons between the results from the numerical simulations and the experimental measurements are shown in Fig. 7, Fig. 8 and Fig. 9. The numerical predictions for the mean drag coefficient ($\overline{C}_D$), the root mean square lift force coefficient (C_{Lrms}) and the Strouhal number (St) all show good agreements when compared with the experimental data. The drag and lift force coefficients on the structures remain stable in both the numerical and experimental results. The numerically predicted

281 Strouhal number (*St*) is around 0.14 which is similar to the results from the CFD study carried out by

282 Lee et al. (2014).

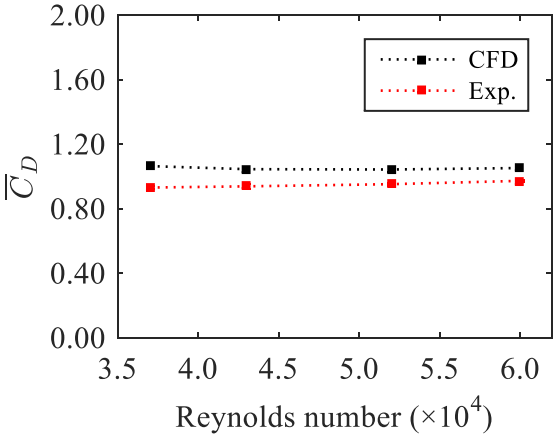

283

284 Fig. 7. Mean drag coefficient ($\overline{C}_D$) from the numerical and experimental results for the stationary

285 model.

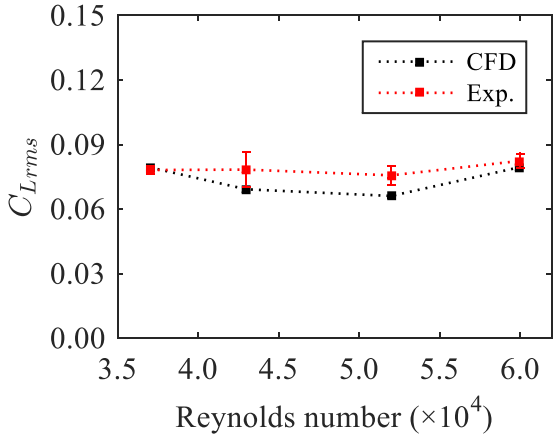

286

287 Fig. 8. Root mean square lift coefficient (C_{Lrms}) from the numerical and experimental results for the

288 stationary model.

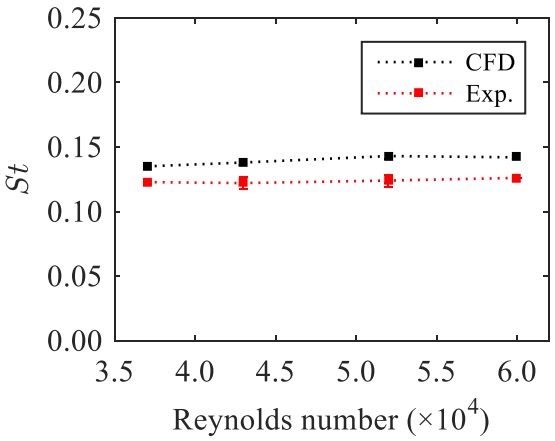

289

290 Fig. 9. Strouhal number (*St*) from the numerical and experimental results for the stationary model.

291 3.2.2. Drag and lift forces on each member of the DDS

292 In order to improve the understanding of interactions between vortex shedding processes due to each
293 structure member of the DDS, the drag and lift force coefficients on each member of the DDS are
294 calculated and presented in Fig. 10, Fig. 11 and Fig. 12. The mean drag coefficients on each member
295 remain stable within the current Reynolds number range similar to the trend of the overall mean drag
296 coefficients on the DDS as discussed in the above section. Respectively, the upstream column
297 (Column 1) experiences a larger mean drag coefficient ($\overline{C}_D$) than the downstream one (Column 3).
298 The portside and starboard side columns (Column 2 and 4) are symmetrically expose to the flow and
299 experience a slightly larger mean drag coefficient ($\overline{C}_D$) than the upstream column, and the pontoon
300 shows the same trend as the side columns do. It is noted that the downstream column and the two side
301 columns are subjected to higher fluctuating lift force coefficient than the upstream one with the
302 downstream column experiencing the largest fluctuating lift force coefficient among all parts of the
303 DDS. The root mean square lift force coefficients on the two side columns are slightly less than that
304 on the downstream one, but still much larger than that on the upstream column. These results show
305 the influence of unsteady vortices and their interactions on the structure members in the downstream.
306 Similar observation was also reported by Lam et al. (2003b).

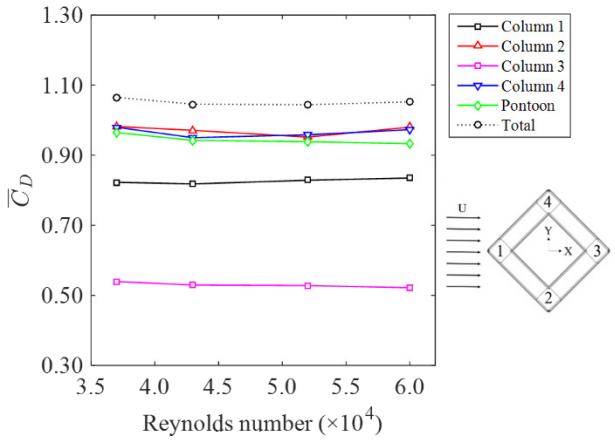

307

308 Fig. 10. Mean drag coefficients ($\overline{C}_D$) on each member of the stationary DDS.

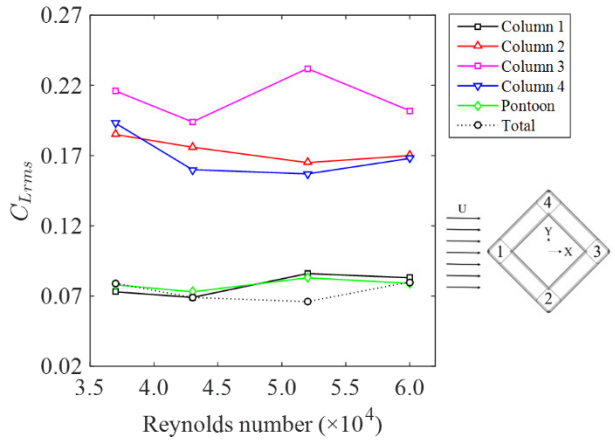

309

310 Fig. 11. Root mean square lift coefficients (C_{Lrms}) on each member of the stationary DDS.

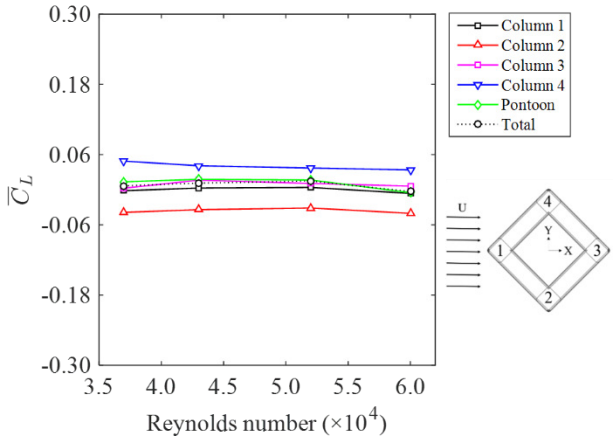

311

312 Fig. 12. Mean lift coefficient ($\overline{C}_L$) on each member of the stationary DDS.

313 3.2.3. Flow patterns and the lift force time history

314 With the aim to reveal the force dynamic behaviours on the structure, the time histories of the lift
315 force coefficients corresponding with the flow patterns at $Re = 4.3 \times 10^4$ are presented in Fig. 13, Fig.
316 14 and Fig. 15.

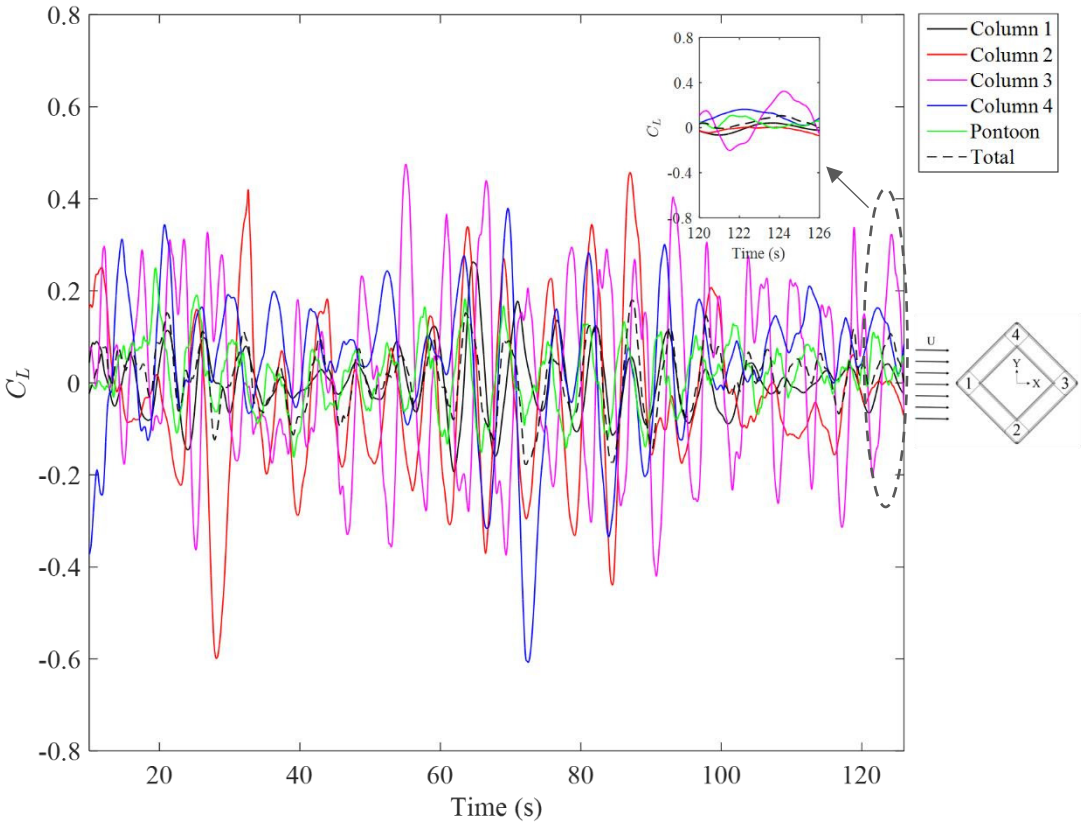

317

318 Fig. 13. Lift force coefficient time history on different members of the DDS at $Re = 4.3 \times 10^4$,
319 including locally zoomed in the last 6s.

320 As can be seen in Fig. 13, the time history of the lift force coefficient on column 3 shows a hysteresis
321 phenomenon which indicates the lift force oscillating period on column 3 always delayed compared
322 with other structure members. The peak values of the lift coefficient on column 3 are almost

corresponded to the bottom values of other structure members, and vice versa. From the pressure contours (Fig. 14), it can be clearly observed that there is a relatively stationary high pressure zone in front of column 1, 2 and 4. However, the high pressure zone in front of the downstream column 3 keeps changing along with the vortex shedding processes. The fluctuations of the pressure in front of column are primarily induced by the impingement of the upstream generated vortices, and these fluctuations of the pressures cause the downstream column 3 to have higher C_{Lrms} and lower $\overline{C}_D$ values compared with other three upstream columns. On the other hand, the pressure fluctuations in front of column 3 are mainly resulted in the interaction between the vortices shed from the upstream column 1 and the shear layers separated from the downstream column 3, which can be clearly seen in Fig. 15. Similar observations were also noted by Ljungkrona et al. (1991), Chen and Chiou (1997) and Liu and Chen (2002).

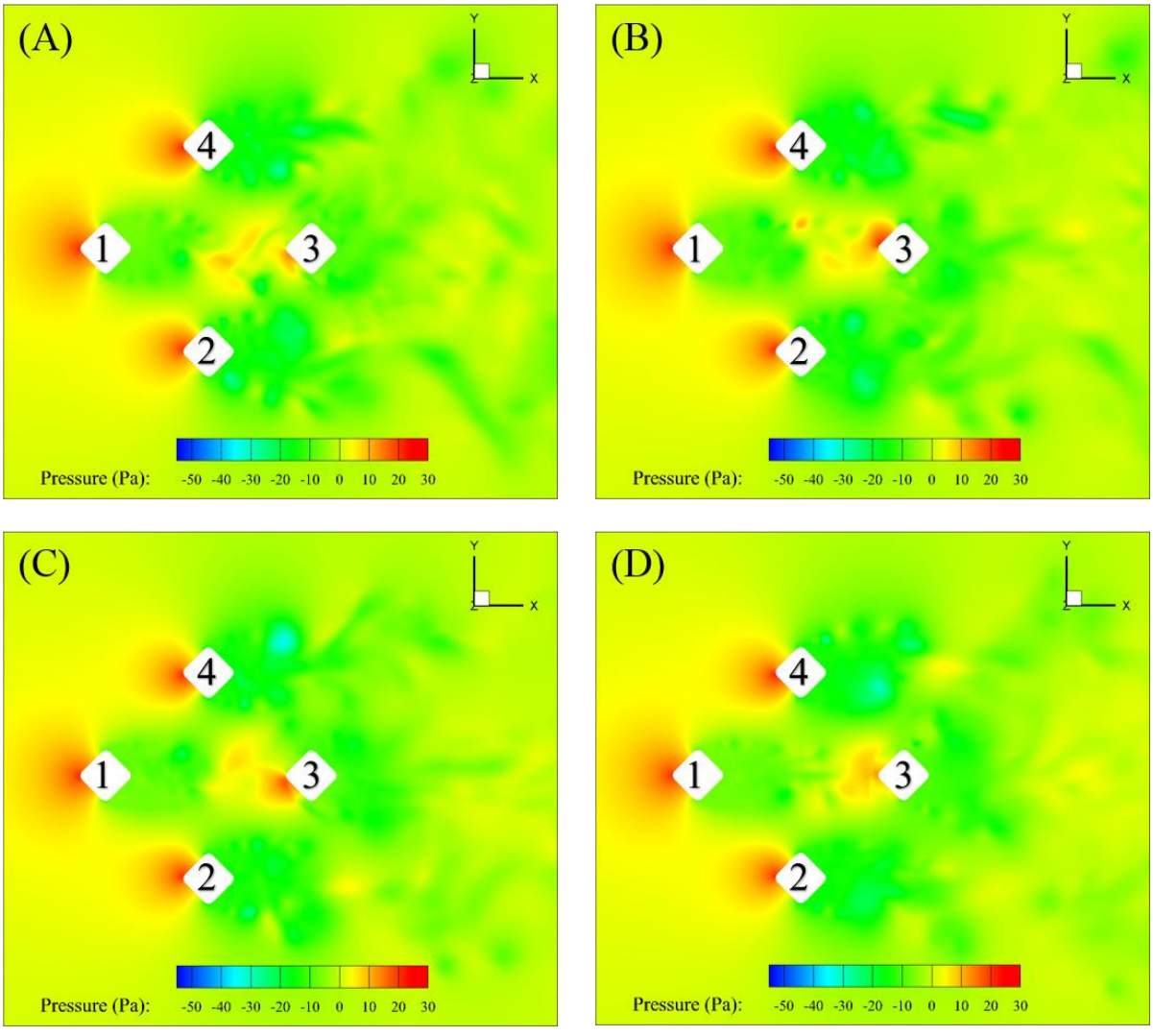

Fig. 14. A time series of the pressure distribution around the DDS at middle draft showing the instantaneous flow fields around the DDS at $Re = 4.3 \times 10^4$ corresponding to the lift force coefficient time history (A: 120.6s; B: 122.4s; C: 124.2s; D: 126.0s).

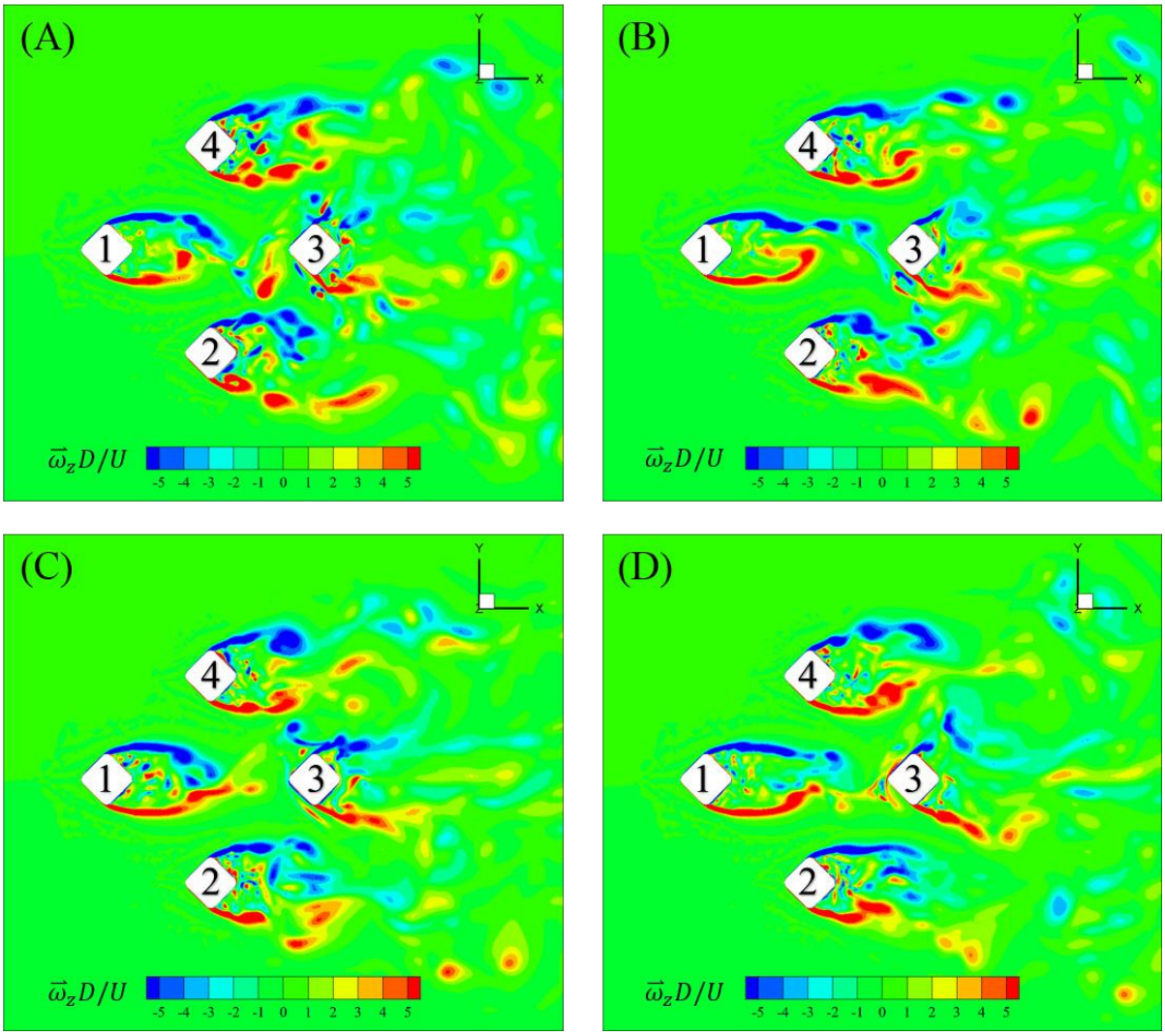

Fig. 15. A time series of non-dimensional spanwise vorticity ($\vec{\omega}_z D/U$) contours around the DDS at the middle draft level showing the instantaneous flow fields around the DDS at $Re = 4.3 \times 10^4$ corresponding to the lift force coefficient time history (A: 120.6s; B: 122.4s; C: 124.2s; D: 126.0s).

Fig. 15 also shows that the vortex shedding patterns due to each column are very different. It is seen that very slim vortices are shed from the corners of column 1. However, the vortices shed from the two side columns, i.e., column 2 and column 4 appear to be not as slim as the ones of column 1, and

345 even shorter vortices shed from the corners of downstream column 3 are clearly visible. Moreover,
346 column 2 and column 4 shed the large vortices symmetrically, where column 2 shed the vortices on its
347 portside corner and the column 4 shed on its starboard side corner. This symmetrical vortex shedding
348 pattern contributes to the symmetrical values of $\overline{C}_L$ for column 2 and column 4 as shown in Fig. 12.

349 3.3. VIM model results and observations

350 After studying the vortex shedding interactions with the columns for the flow over a stationary
351 structure, a VIM investigation was carried out, in order to reveal the cause of VIM by comparing the
352 forces distributions and the flow patterns differences between the flow over the motion-coupled
353 structure cases with the stationary structure cases.

354 In this section, the numerical simulations of the flow over a three degree of freedom deep-draft semi-
355 submersible model with different Reynolds numbers from 3.6×10^4 to 1.1×10^5 are carried out to
356 investigate the overall hydrodynamics of the structure. Results for all cases are obtained by averaging
357 after more than ten vortex shedding cycles. Although the sample size is relatively small, the reliability
358 and sensitivity of the relatively small data set on the results have been discussed by Zhang et al.
359 (2014). These numerical predictions are subsequently validated by the motion and force
360 measurements obtained from the corresponding experiments undertaken in a towing tank. The
361 characteristics of vortex shedding processes and their interactions due to multiple cylindrical columns
362 are also discussed.

363 3.3.1. Experimental test

364 Table 5. Natural periods of the motions in calm water.

Incidence (°)	**Natural period of transverse motion,** $T_{0transverse}$ **(s)**	**Natural period of in-line motion,** $T_{0in\text{-}line}$ **(s)**	**Natural period of yaw motion,** T_{0yaw} **(s)**
45°	20.1	19.2	18.3

In order to validate the numerical model, a series of experiments were performed in a towing tank with a dimension of 130 × 6 × 3m (length × width × depth). The model II described in Table 1 was tested under a reduced velocity (*Ur*) ranging from 3.4 to 14.1. A minimum of ten oscillation cycles were allowed to occur in order to reach the quasi-steady state of the VIM phenomenon. Only three degrees of freedom (namely transverse, in-line and yaw) were allowed in the experiments. The motion time histories were recorded and the forces on mooring lines were measured to obtain the hydrodynamic loads on the model. Table 5 lists the natural periods of the motions in calm water obtained from the decay tests.

3.3.2. Motion characteristics

The non-dimensional characteristic amplitudes are introduced in this section to describe and present the VIM motion characteristics. The non-dimensional characteristic amplitudes are defined as:

$$A_x/L = \sqrt{2} \times \sigma\left(\frac{x(t)}{L}\right), \tag{5}$$

$$A_y/L = \sqrt{2} \times \sigma\left(\frac{y(t)}{L}\right), \tag{6}$$

$$Yaw_{nom} = \sqrt{2} \times \sigma(yaw(t)), \tag{7}$$

where L is the column width, σ is the standard deviation obtained from the time series, $x(t)$, $y(t)$ and $yaw(t)$ represent the in-line, transverse and yaw motions time series respectively.

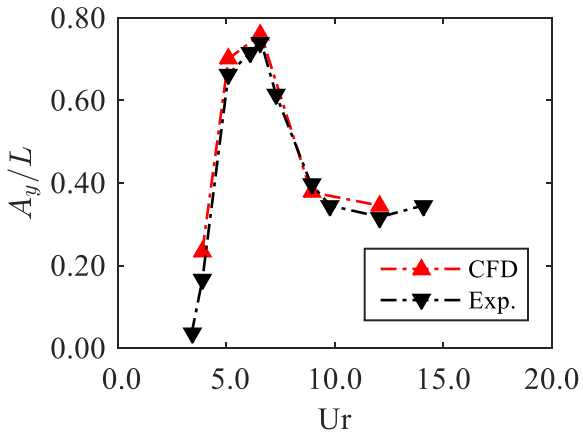

Fig. 16. Non-dimensional transverse characteristic amplitudes (A_y/L), the *Ur* is defined based on the natural period of the transverse motion.

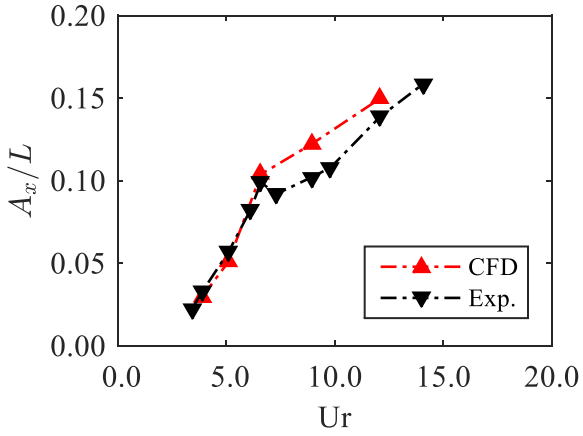

Fig. 17. Non-dimensional in-line characteristic amplitudes (A_x/L), the *Ur* is defined based on the natural period of the transverse motion.

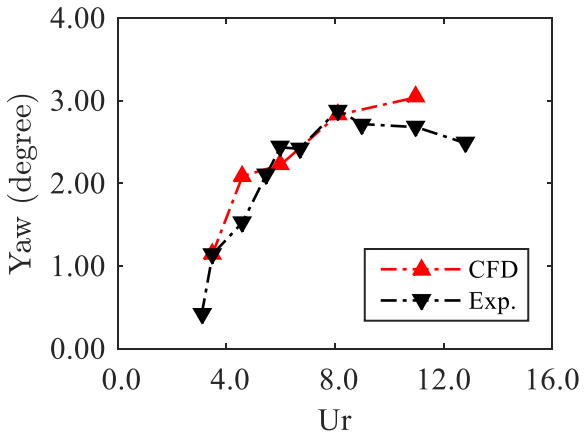

387

388 Fig. 18. Non-dimensional yaw characteristic amplitudes, the *Ur* is defined based on the natural period
389 of the yaw motion.

390 Fig. 16, Fig. 17 and Fig. 18 present the non-dimensional transverse, in-line and yaw motion
391 amplitudes obtained from the numerical simulations and the experimental measurements. In each
392 case, the numerical predictions show a good agreement with the experimental results. However, at
393 low *Ur* values, the numerical simulation predicts a slightly larger transverse response than the
394 experimental data. An analysis of the error will be given in the following 3.3.3. Force analysis section
395 together with the added mass analysis. From the non-dimensional transverse characteristic amplitude
396 in Fig. 16, the "lock-in" phenomenon can be clearly seen occurring in a reduced velocity range from 5
397 to 9. The transverse motion increased rapidly from the "pre lock-in" region to the "lock-in" region,
398 and then sharply declines from the "lock-in" region to the following "post lock-in" region. The peak
399 point for the transverse motion is at $Ur = 6.6$.

400 3.3.3. Force analysis

401 In order to study the fluctuation forces responsible for VIM, the lift and drag forces and the related
402 coefficients are further analysed. Fig. 19 and Fig. 20 show the mean drag force coefficient ($\overline{C}_D$) and
403 the root mean square lift force coefficient (C_{Lrms}) respectively as a function of the reduced velocity
404 (Ur) for both numerical and experimental results. The numerical method predicts well compared with

the experimental measurements. However, there is a discrepancy between the numerical predictions and the experimental data at low reduced velocity levels for the root mean square lift force coefficient, similar to the trend observed in the non-dimensional transverse characteristic amplitudes in Fig. 16.

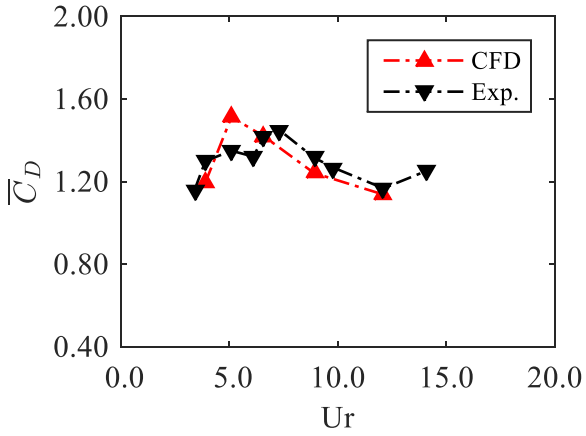

Fig. 19. Mean drag coefficient ($\overline{C}_D$) from the numerical and experimental results on the VIM model, the *Ur* is defined based on the natural period of the transverse motion.

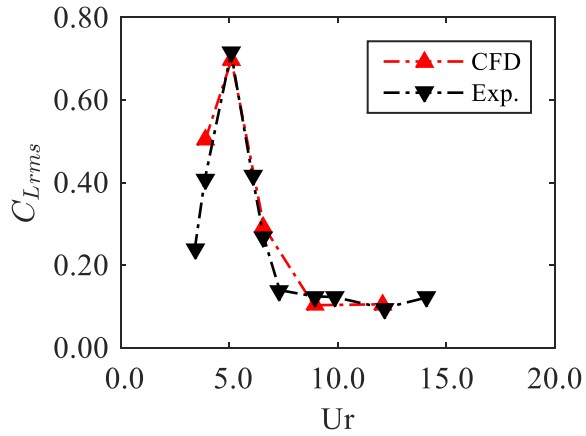

Fig. 20. Root mean square lift coefficient (C_{Lrms}) from the numerical and experimental results on the VIM model, the *Ur* is defined based on the natural period of the transverse motion.

To further examine the differences, a virtual variable so-called added mass coefficient (C_a) has been introduced to compare the differences between the numerical predictions and the experimental

measurements. Similar to the discussions made by Sarpkaya (2004) in their vortex-induced vibrations study, Zhang et al. (2014) introduced this variable into a Spar VIM investigation. In their work, the added mass coefficient (C_a) is estimated by the equations proposed by Vikestad et al. (2000) as follows:

$$C_a = \frac{m_a}{\rho\Delta}, \tag{8}$$

$$C_a = -\frac{2}{nT\rho\Delta\left(\sqrt{2}rms(\ddot{y})\right)^2}\int_t^{t+nT} F_y\ddot{y}dt, \tag{9}$$

where n is an integer number of oscillation periods, nT is the time length, ρ is the fresh water density, Δ is the displacement of the structure, F_y is the cross-flow component of the total hydrodynamic force on the structure and y is the transverse displacement of the motion.

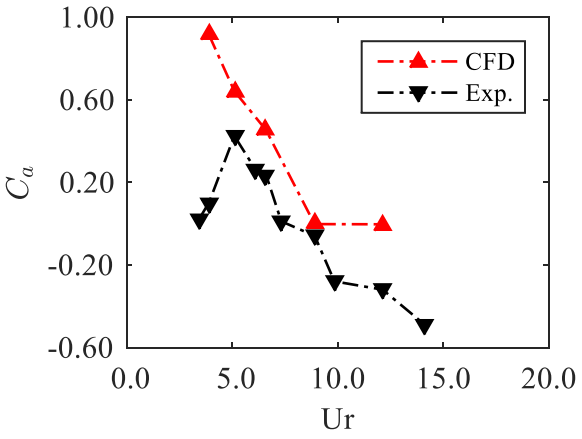

Fig. 21. Added mass coefficient (C_a) of the VIM model from the numerical predictions and the experiments, the Ur is defined based on the natural period of the transverse motion.

Fig. 21 shows the comparison of the added mass coefficients (C_a) obtained from the numerical calculations and the experiments. The numerical prediction shows a decreasing trend similar to that reported in an earlier study by Zhang et al. (2014). This trend is also the same as the results from the studies conducted by Sarpkaya (2004). However, the added mass coefficient (C_a) obtained from the

experimental measurements at low reduced velocity range are significantly different to those from the present numerical predictions. A distinct feature shown in Fig. 21 is that the added mass coefficient from experiments is much smaller at very low *Ur* and trends to increase initially and then decrease rapidly with the increases of the reduced velocity. The apparent discrepancy between the numerical and experimental results at low reduced velocities is likely to be caused by the experimental data. There are a few possibilities that could cause the error. Firstly, the towing speed during the experiment is extremely low for an equivalent low reduced velocity (for example, 0.073m/s for reduced velocity at $Ur = 3.4$), and the whole system mechanical friction may affect the experimental measurements at such a low towing speed; secondly, the influence of the mooring line settings may also affect the experimental measurements, because the theoretically linear springs set in numerical simulations are ideal springs and the mooring lines in the experimental set-up may not be arranged as symmetrically as in the numerical simulations. Due to these factors, the numerical results may be more reliable and accurate than the experimental data in the low reduced velocity range.

Similar to the motion observation, the "lock-in" phenomenon can also be seen in Fig. 19 and Fig. 20. However, it is noted that the "lock-in" phenomenon in the force domain is seen to occur slightly earlier than in the transverse motion domain, as also observed by Gonçalves et al. (2012) in their experiments. The peak point for the drag and lift force coefficients in the present study are at $Ur = 5.1$ while the peak point for the transverse motion is at $Ur = 6.6$.

Both the transverse motion time histories and the lift force coefficient time histories are transferred from the time domain to the frequency domain by using the Fast Fourier transform (FFT) in order to study the "lock-in" phenomenon. The frequency domain results are shown in Fig. 22 to Fig. 26, inclusive the "pre lock-in", "lock-in" and "post lock-in" regions. The transverse motion frequency and vortex shedding frequency are both close to the transverse natural frequency in still water at the "pre lock-in" and "lock-in" regions. The oscillation and vortex shedding frequency are shown increasing with the increase in reduced velocity. When the "post lock-in" started, the oscillation frequency and vortex shedding frequency started to be further away from the transverse motion natural frequency as

can be seen in Fig. 25. For the highest reduced velocity case at *Ur* = 12.1, Fig. 26 shows multiple peak frequencies appearing in the frequency domain.

As can be seen in Fig. 22 to Fig. 25, the agreement between the numerical predictions and the experimental measurements for both transverse motions and the lift force coefficients are reasonably well. It is seen that in Fig. 26, however, at "Ur = 12.1", the agreement is less well especially the magnitudes of motion and force coefficient though the dominant frequencies were still predicted accurately. It is noted that, at such a high reduced velocity (Ur = 12.1) far beyond the "lock-in" region (approx. Ur = 6.6), the magnitudes of the transverse motion and lift force coefficient are much smaller, thus, the relatively larger discrepancies appeared in Fig. 26.

Compared to Fig. 24 with *Ur* = 6.6, Fig. 23 shows that the oscillation frequency and vortex shedding frequency are closer to the transverse natural frequency at *Ur* = 5.1, where the values of the peak drag and lift force coefficients appear. Furthermore, the added mass may also contribute to the earlier peak drag and lift force occurrence. Since the added mass keeps decreasing with the reduced velocity increasing, the force domain and the motion domain may have a hysteresis phenomenon which requires further studies.

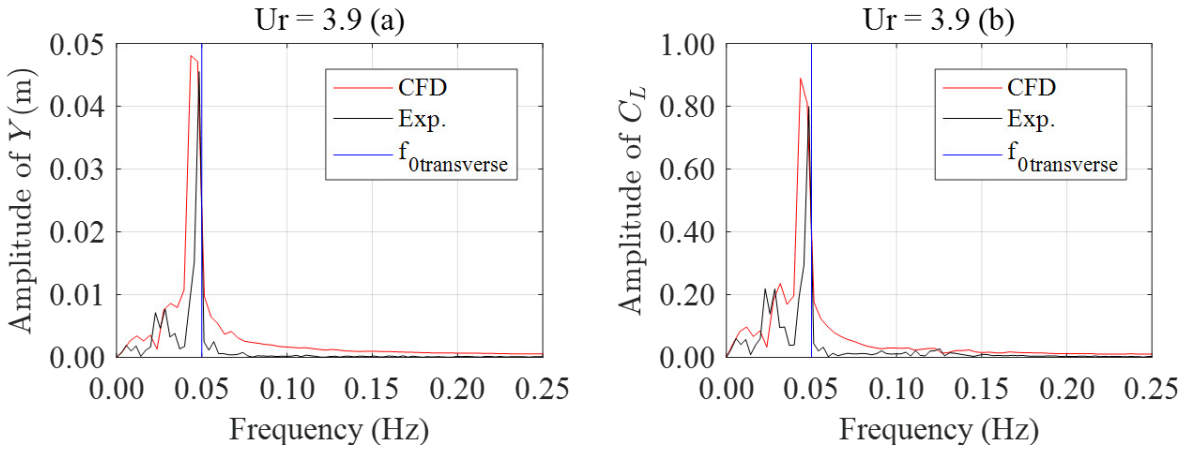

Fig. 22. FFT of the transverse motions and the lift force coefficients at *Ur* = 3.9, (a) transverse motion; (b) lift force coefficient.

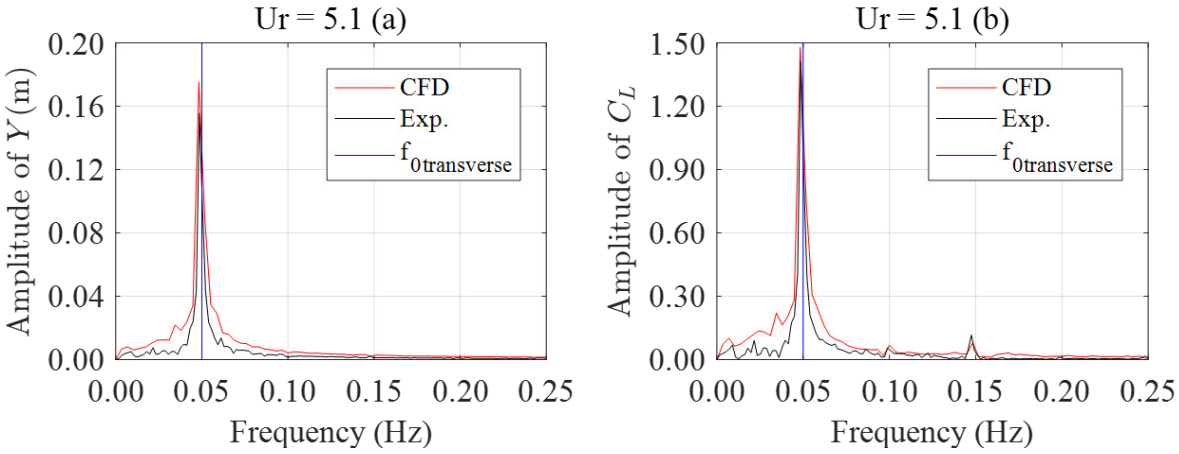

476

477 Fig. 23. FFT of the transverse motions and the lift force coefficients at *Ur* = 5.1, (a) transverse

478 motion; (b) lift force coefficient.

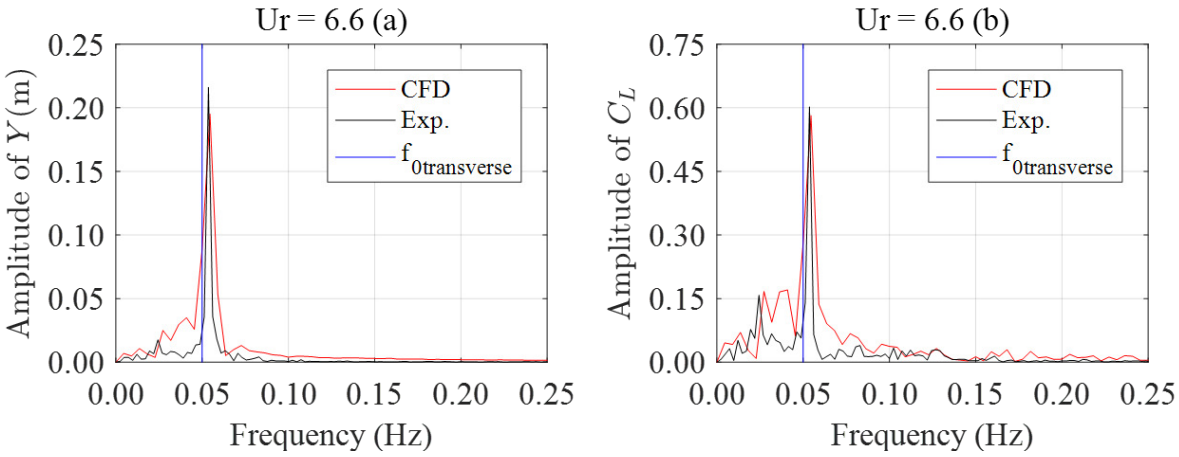

479

480 Fig. 24. FFT of the transverse motions and the lift force coefficients at *Ur* = 6.6, (a) transverse

481 motion; (b) lift force coefficient.

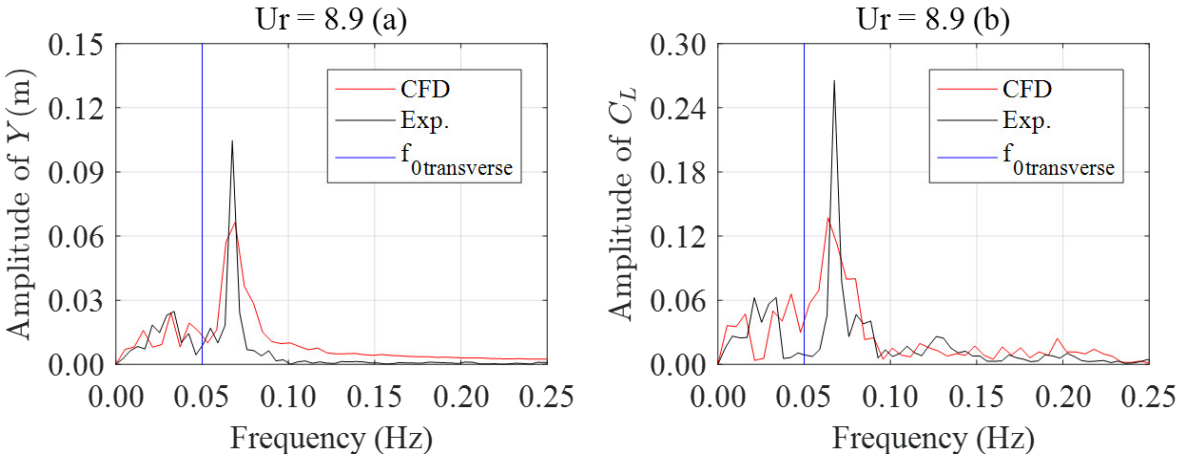

Fig. 25. FFT of the transverse motions and the lift force coefficients at *Ur* = 8.9, (a) transverse motion; (b) lift force coefficient.

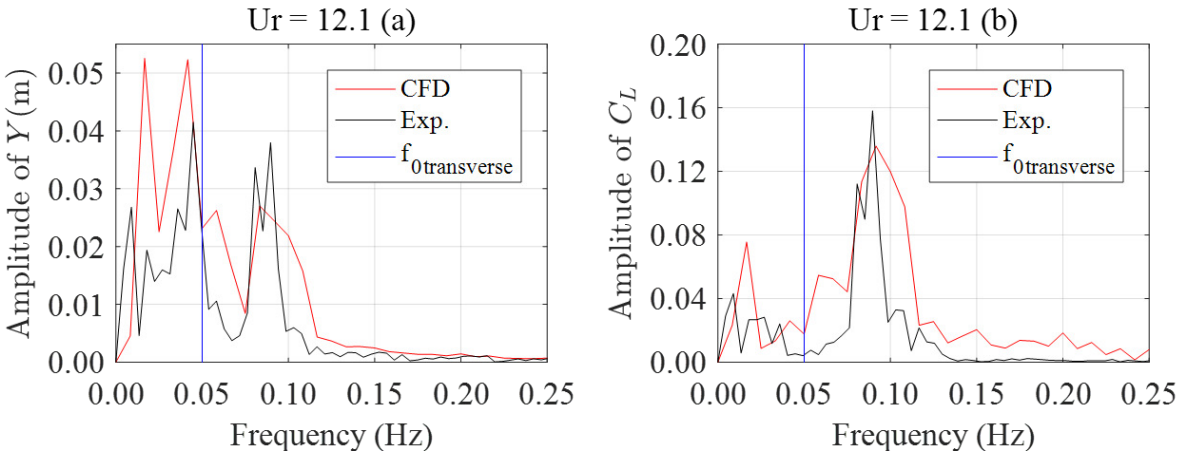

Fig. 26. FFT of the transverse motions and the lift force coefficients at *Ur* = 12.1, (a) transverse motion; (b) lift force coefficient.

To examine the complex fluid mechanisms on the structure and the corresponding motion driven parts of the structure, the drag and lift force coefficients on different structure members of the DDS are further calculated and analysed.

Unlike the stationary model, the drag and lift force coefficients are changed when the reduced velocity increases (Fig. 27 and Fig. 28). The mean drag coefficient ($\overline{C}_D$) on the upstream column

(Column 1), the portside column (Column 2) and the starboard side column (Column 4) are excited by the "lock-in" phenomenon. The pontoons are less excited compared to the three aforementioned columns. However, the drag force coefficient on the downstream column (Column 3) is decreasing while coefficients for the other members experiencing increasing trends and only recovers when "post lock-in" phase starts. The drag force coefficient on the downstream column is also much smaller than that for other members of the structure. On the other hand, the lift force coefficient (C_{Lrms}) on the downstream column, the portside and starboard side columns, and on the pontoons, are all excited by the "lock-in" phenomenon. At this time, the leading upstream column shows a different trend. The lift force coefficient on the upstream column is seen to decrease while an increasing trend is observed for the other components, and conversely starts to recover as the other components begin to decrease. This is due to the wake region changing behind each of the columns. Further details will be discussed in the 3.3.4. Flow pattern section.

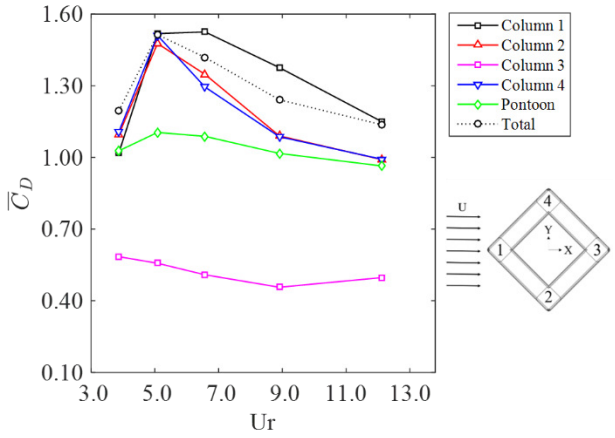

Fig. 27. Mean drag coefficients ($\overline{C}_D$) on each member of the DDS from the VIM model.

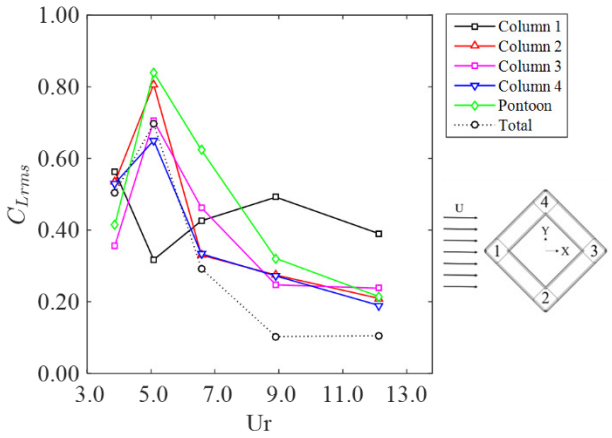

507

508 Fig. 28. Root mean square lift coefficients (C_{Lrms}) on each member of the DDS from the VIM model.

509 The drag and lift forces on the structure are nearly symmetric except the lift force coefficient
510 distribution at Ur = 5.1. Due to the results being based on the motion-coupled simulations, the rigid
511 body motion also needs to be included in the analysis. With this aim, the work done by each member
512 of the structure during the stabilized VIM time is calculated and the results are presented in Fig. 29.
513 The work done is calculated using the following equations:

514 $$W = F \cdot S, \tag{10}$$

515 where F is the total drag and lift force of the structure and S is the displacement of the structure
516 motion.

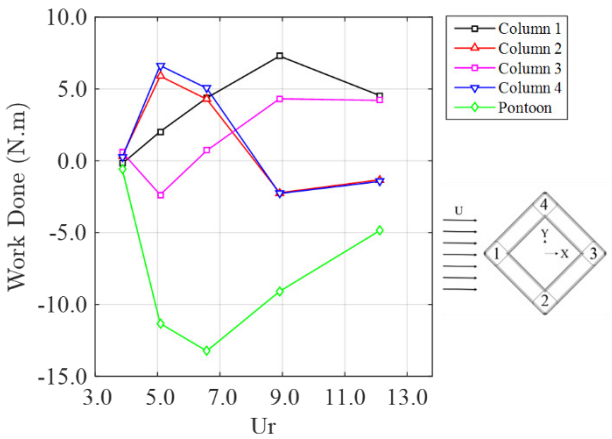

517

Fig. 29. Work done by each member of the DDS on VIM model.

In Fig. 29, the symmetrical characteristics can be clearly identified, and the following features can be observed:

1) The pontoon reduces the VIM response throughout the reduced velocity range. Thus, adding on the pontoon into the overall structure is a good design for restraining VIM responses.

2) The three upstream columns excite VIM responses. Further, the portside and starboard side columns excite VIM responses in the "lock-in" region and trend to resist VIM responses in the "post lock-in" region.

3) The downstream column shows a different trend compared to the portside and starboard side columns; the work done by the downstream column drops initially and then recovers.

3.3.4. Flow pattern

In order to have a general visual appreciation of the vortex shedding patterns, the vorticity contours are plotted in Fig. 31 to Fig. 40. Two non-dimensional variables (non-dimensional vorticity and non-dimensional spanwise vorticity) are used to describe the vorticity in the current study.

$$\text{non-dimensional vorticity} = \omega D/U, \tag{11}$$

$$\omega = \sqrt{\vec{\omega}_x^2 + \vec{\omega}_y^2 + \vec{\omega}_z^2}, \tag{12}$$

$$\text{non-dimensional spanwise vorticity} = \vec{\omega}_z D/U, \tag{13}$$

where, ω is the vorticity magnitude, $\vec{\omega}_x$, $\vec{\omega}_y$ and $\vec{\omega}_z$ are the x, y, and z components of the vorticity, D is the projected length of the column and U is the current speed.

For convenience in describing the vortex development processes, four regions are defined around the column, named as NW (Northwest), NE (Northeast), SW (Southwest) and SE (Southeast) (see Fig. 30). The vortices shed from each side of the column are denoted in chronological order of genesis (e.g., A1, A2 …) from the upper side of Column 1, see Table 6.

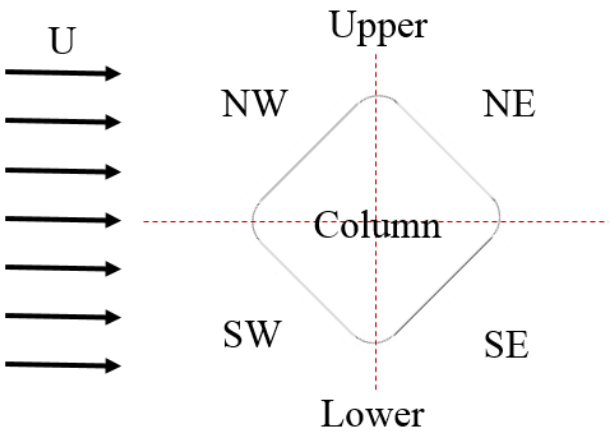

Fig. 30. Definition of the regions around the individual column.

Table 6. The chronological order of vortices genesis for each column.

Column	Shear layer	Vortex street
1	Upper	A1, A2 …
	Lower	B1, B2 …
2	Upper	C1, C2 …
	Lower	D1, D2 …
3	Upper	E1, E2 …
	Lower	F1, F2 …
4	Upper	G1, G2 …
	Lower	H1, H2 …

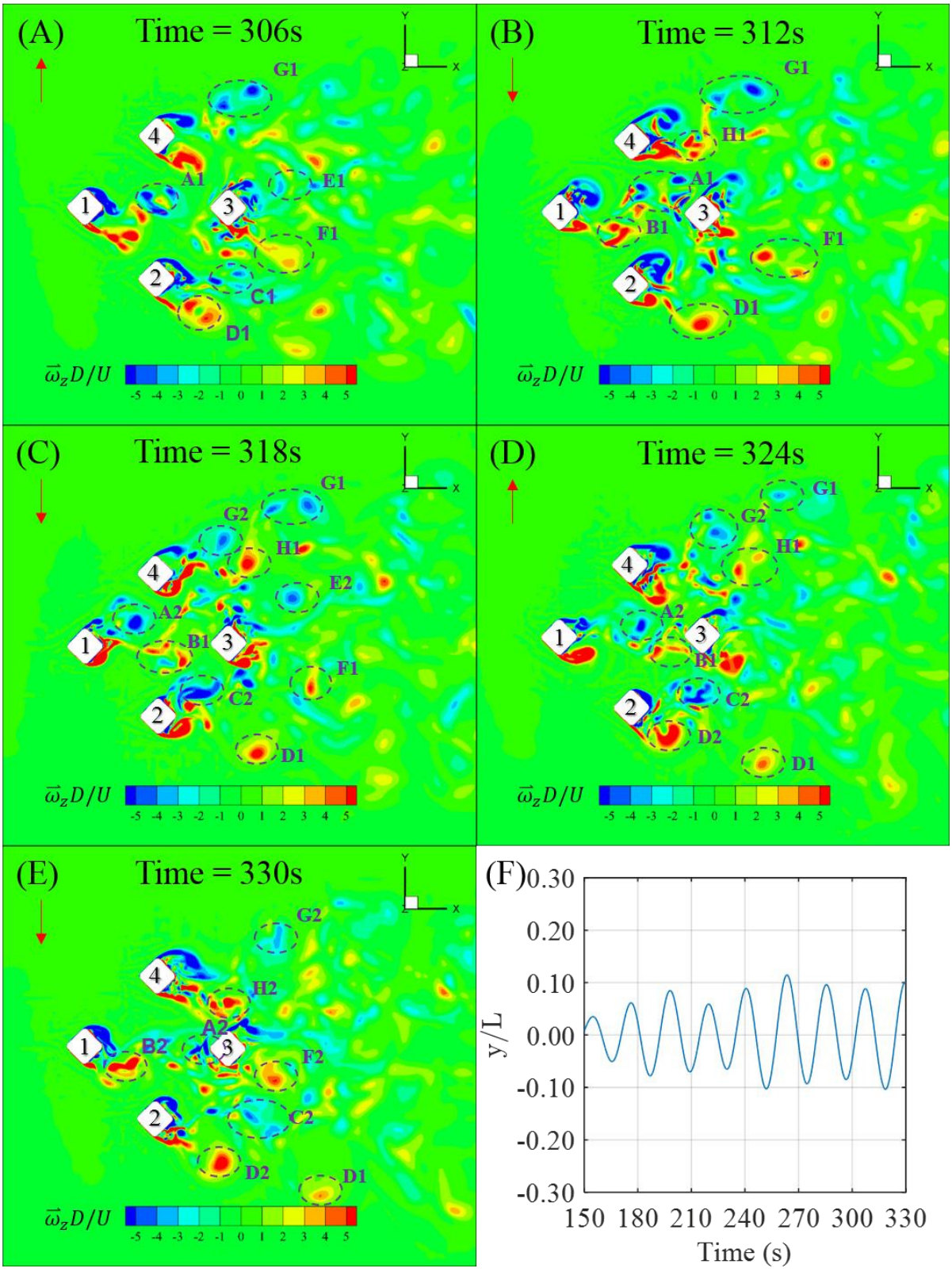

544

545 Fig. 31. A time series of the non-dimensional spanwise vorticity ($\vec{\omega}_z D/U$) contours around the DDS at

546 middle draft showing the instantaneous flow fields around the DDS at *Ur* = 3.9 (A, B, C, D, E) and

the non-dimensional transverse motion (y/L) time history (F); the red arrow is the DDS transverse velocity direction.

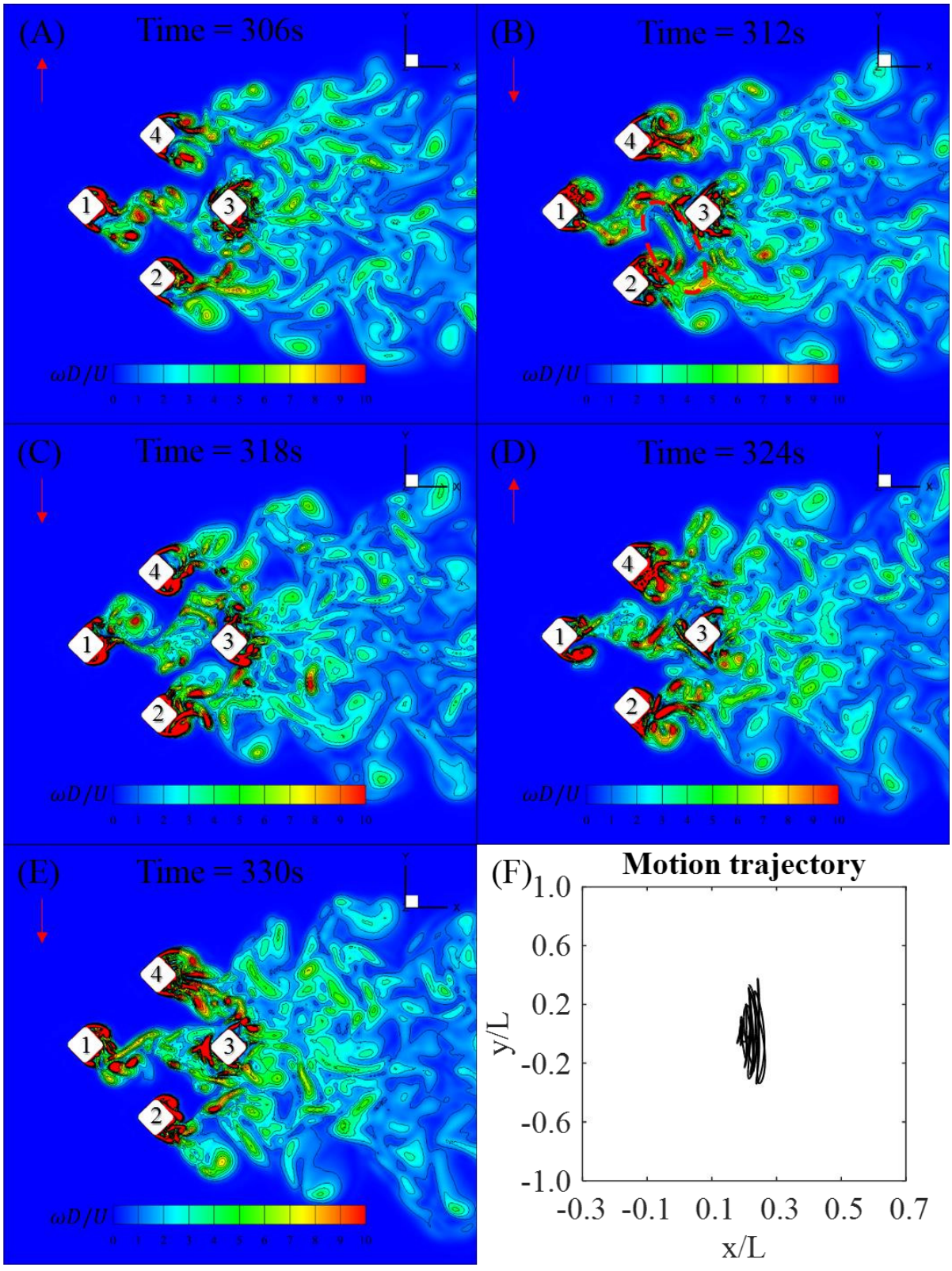

Fig. 32. A time series of the non-dimensional vorticity ($\omega D/U$) contours around the DDS at middle draft showing the instantaneous flow fields around the DDS at Ur = 3.9 (A, B, C, D, E) and the non-dimensional motion trajectory (F); the red arrow is the DDS transverse velocity direction.

Fig. 31 presents the non-dimensional spanwise vorticity ($\overrightarrow{\omega}_z D/U$) contours at Ur = 3.9. As can be seen, the vortices shed from the upstream column (Column 1) directly impinge on the downstream column (Column 3) and then join into the downstream column's weak region. The vortex street can be clearly found behind the upstream column where the "2S" type shedding occurs. Additionally, the vortices shed from the portside and starboard side columns (Column 2 and 4) also impinge on the downstream column, which are red circled in Fig. 32(B). These vortex patterns are not visible in the spanwise vorticity contour (Fig. 31) indicating that there are three-dimensional effects on the flow characteristics especially on the side columns' wake region and the flow region in front of the downstream column.

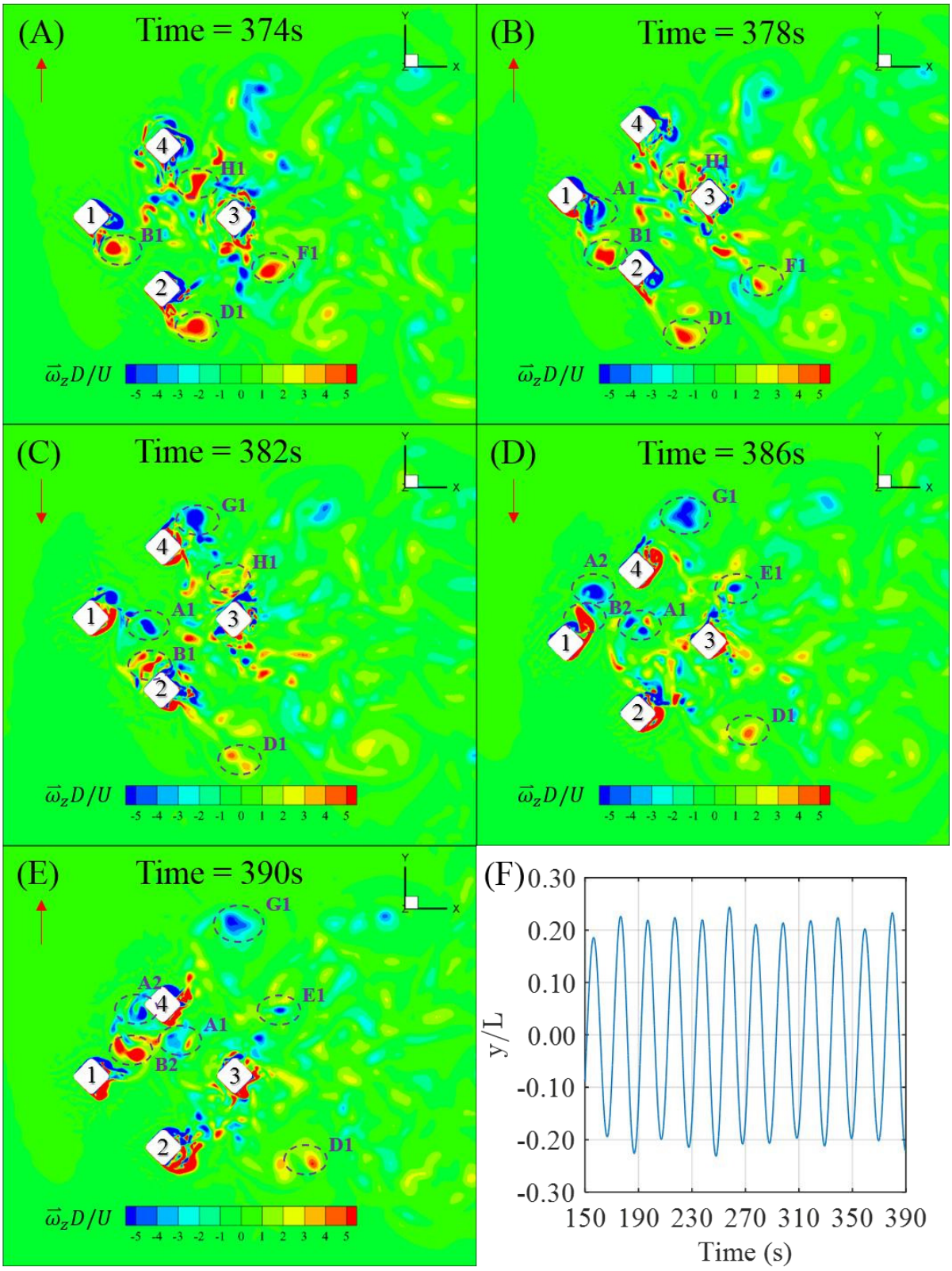

Fig. 33. A time series of the non-dimensional spanwise vorticity ($\vec{\omega}_z D/U$) contours around the DDS at middle draft showing the instantaneous flow fields around the DDS at Ur = 5.1 (A, B, C, D, E) and

565 the non-dimensional transverse motion (y/L) time history(F); the red arrow is the DDS transverse

566 velocity direction.

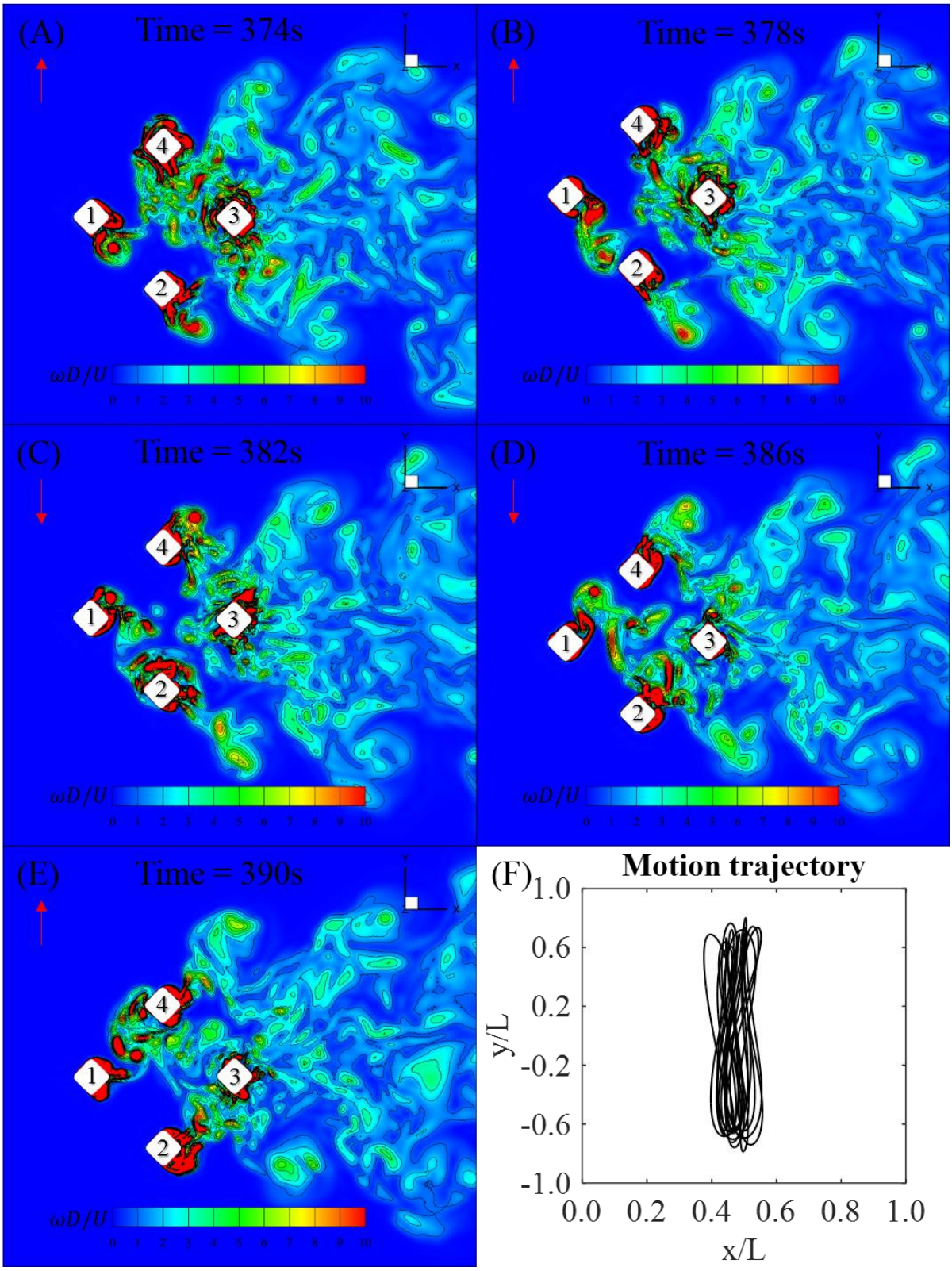

567

Fig. 34. A time series of the non-dimensional vorticity ($\omega D/U$) contours around the DDS at middle draft showing the instantaneous flow fields around the DDS at Ur = 5.1 (A, B, C, D, E) and the non-dimensional motion trajectory (F); the red arrow is the DDS transverse velocity direction.

With the increase of the Ur, in the "lock-in" region, the flow patterns are changed. When Ur = 5.1, the structure oscillation frequency is close to the natural frequency of the structure in still water. As the result of the resonance developing, the motion starts to amplify and the flow patterns are changed significantly. Vortex streets only appear on the opposite of the transverse velocity direction (see Fig. 33 and Fig. 34). The vortices shed from the upstream column (Column 1) where the "P+S" type shedding occurred periodically and symmetrically impinge on the portside and starboard side (Column 2 and 4). Respectively, the vortices generated by the upstream column impinge on the NW face of the portside column (Column 2) and the SW face of the starboard side column (Column 4). Only one strong vortex will form on the opposite side to the transverse velocity direction behind portside and starboard side columns (see "D1, H1, G1" in Fig. 33). Also, the vortices shed from the side columns impinge on the downstream column (Column 3). As a result, there is no clear vortex street behind the downstream column. Small vortices in piece can be seen in the downstream of Column 3. In addition, the motion trajectory shows a figure "8" shape under Ur = 5.1.

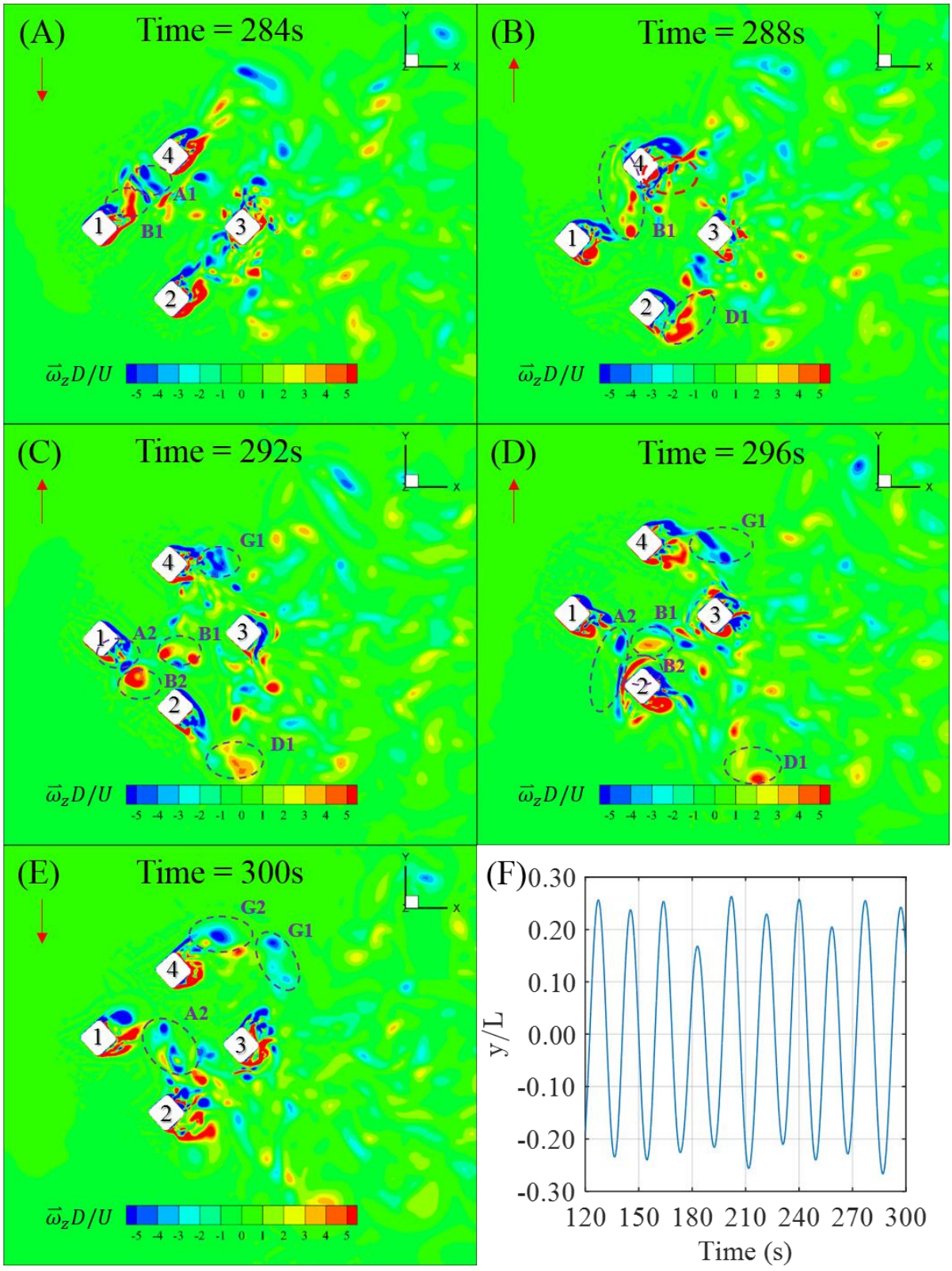

584

585 Fig. 35. A time series of the non-dimensional spanwise vorticity ($\vec{\omega}_z D/U$) contours around the DDS at

586 middle draft showing the instantaneous flow fields around the DDS at *Ur* = 6.6 (A, B, C, D, E) and

the non-dimensional transverse motion (y/L) time history (F); the red arrow is the DDS transverse velocity direction.

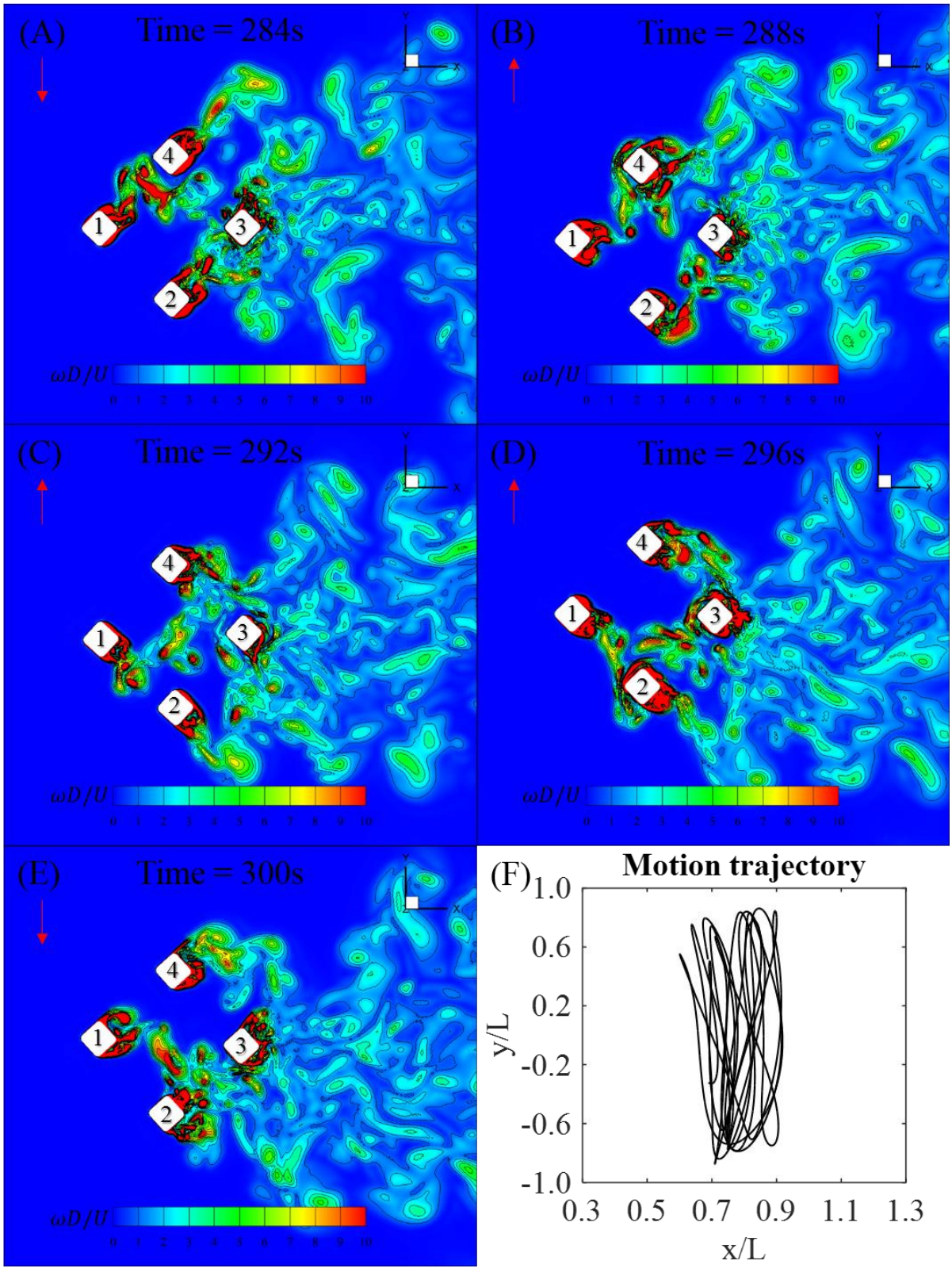

590 Fig. 36. A time series of the non-dimensional vorticity ($\omega D/U$) contours around the DDS at middle
591 draft showing the instantaneous flow fields around the DDS at Ur = 6.6 (A, B, C, D, E) and the non-
592 dimensional motion trajectory (F); the red arrow is the DDS transverse velocity direction.

593 With a further slight increase of the Ur, the transverse motion keeps amplifying. However, the lift
594 force coefficient reduces (see Fig. 16 and Fig. 20). This hysteresis phenomenon can be explained by
595 Fig. 35. As the transverse motion is amplified, after impinging on the starboard side column (Column
596 4), the vortices that are shed from the upstream column (Column 1) move back to impinge on the
597 portside column (Column 2). This can be seen by following the trajectory of the vortices "B1".
598 Additionally, the vortices like "B1" affect the vortices detached from the upper side of Column 2 and
599 lower side of Column 4. As can be seen in Fig. 35(B) (red circled), two different clockwise vortices
600 are mixed together on the SE face of the starboard side column. The mixing of the vortices can
601 decrease the lift force on the structure. This is one of the reasons that makes the lift force coefficient
602 on the structures drops while the transverse motion increases. By comparing the differences between
603 Fig. 33 and Fig. 35, there is another factor which may contribute to the hysteresis phenomenon. In
604 Fig. 35, it is seen that strong vortices are detached from both portside and starboard side at same time.
605 While in Fig. 33, only one strong vortex will form on the opposite side to the transverse velocity
606 direction behind portside and starboard side columns. The differences of the flow characteristics
607 shown in Fig. 33 and Fig. 35 lead to the peak point in the force domain occurs slightly earlier than
608 that in the transverse motion domain.

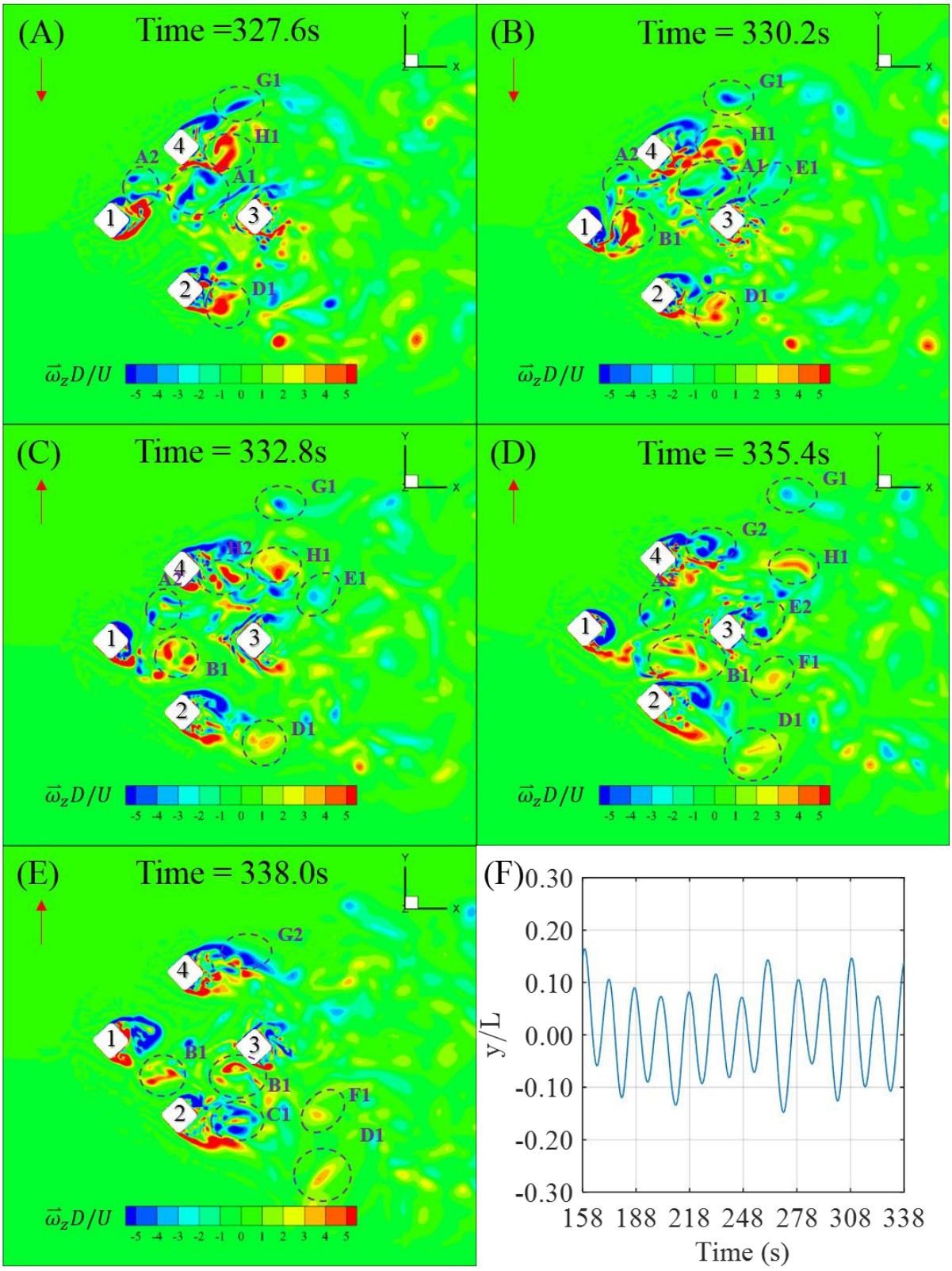

609

610 Fig. 37. A time series of the non-dimensional spanwise vorticity ($\vec{\omega}_z D/U$) contours around the DDS at

611 middle draft showing the instantaneous flow fields around the DDS at *Ur* = 8.9 (A, B, C, D, E) and

the non-dimensional transverse motion (y/L) time history (F); the red arrow is the DDS transverse velocity direction.

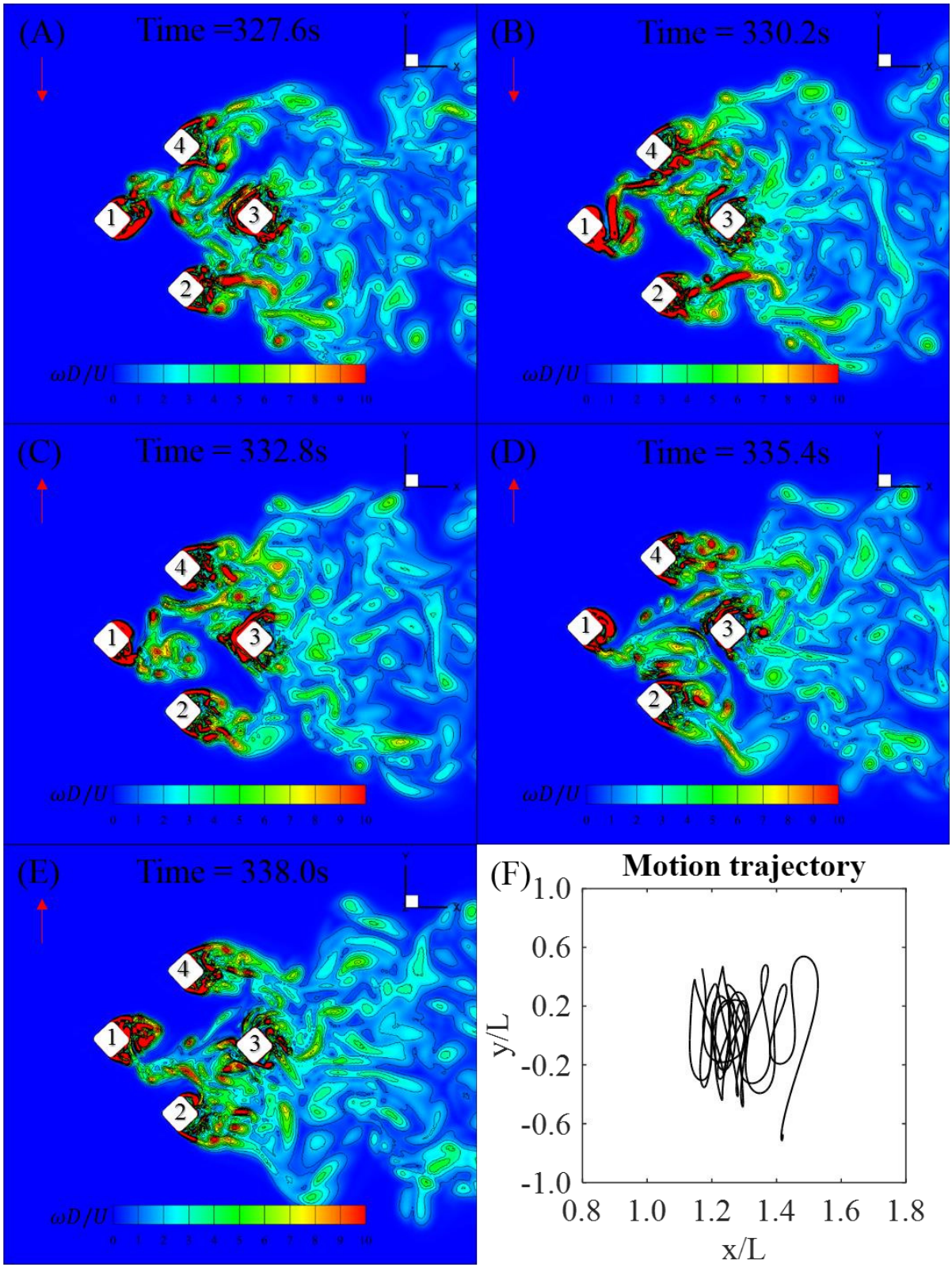

615 Fig. 38. A time series of the non-dimensional vorticity ($\omega D/U$) contours around the DDS at middle
616 draft showing the instantaneous flow fields around the DDS at Ur = 8.9 (A, B, C, D, E) and the non-
617 dimensional motion trajectory (F); the red arrow is the DDS transverse velocity direction.

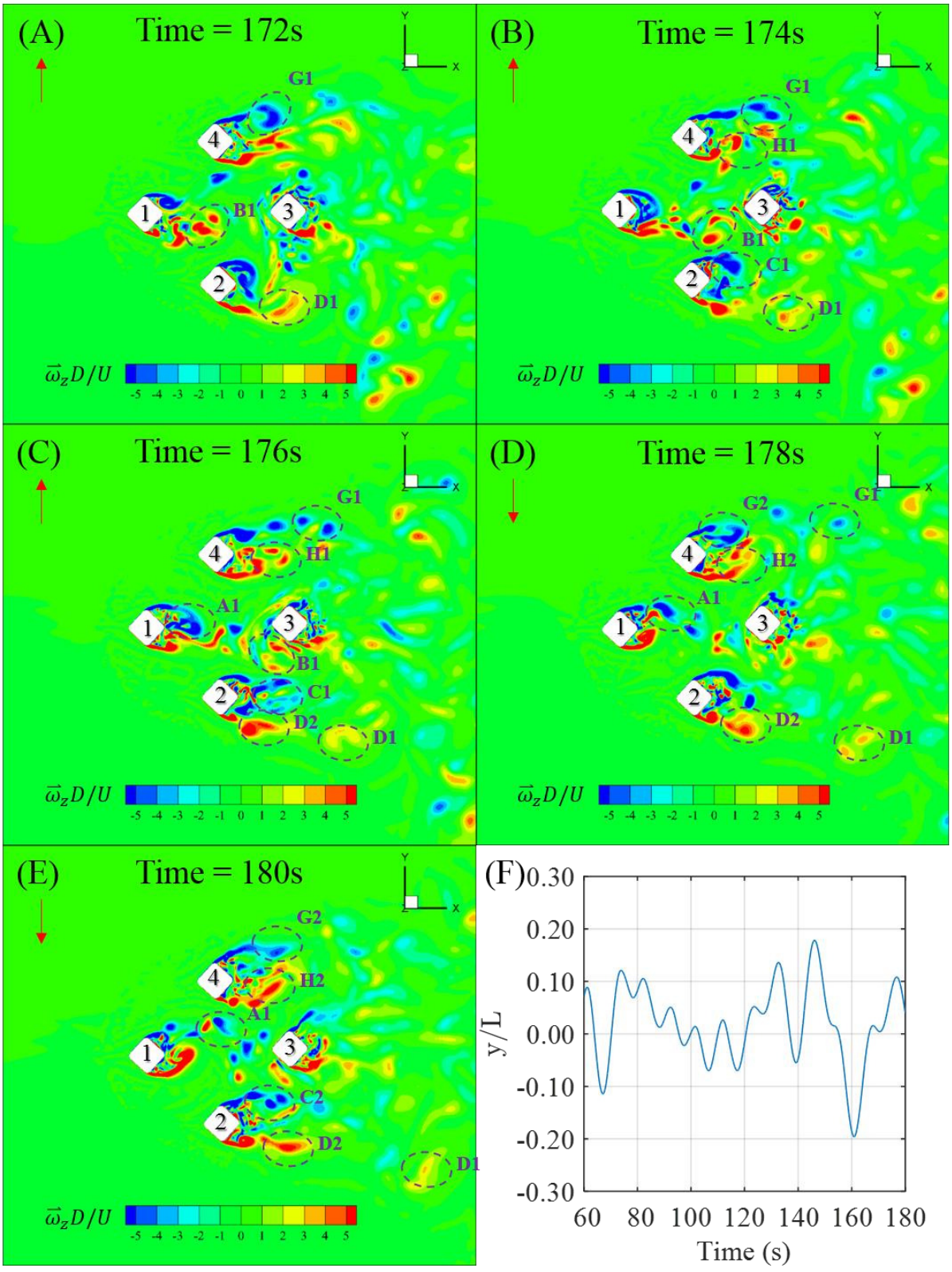

618

619 Fig. 39. A time series of the non-dimensional spanwise vorticity ($\vec{\omega}_z D/U$) contours around the DDS at
620 middle draft showing the instantaneous flow fields around the DDS at Ur = 12.1 (A, B, C, D, E) and
621 the non-dimensional transverse motion (y/L) time history (F); the red arrow is the DDS transverse
622 velocity direction.

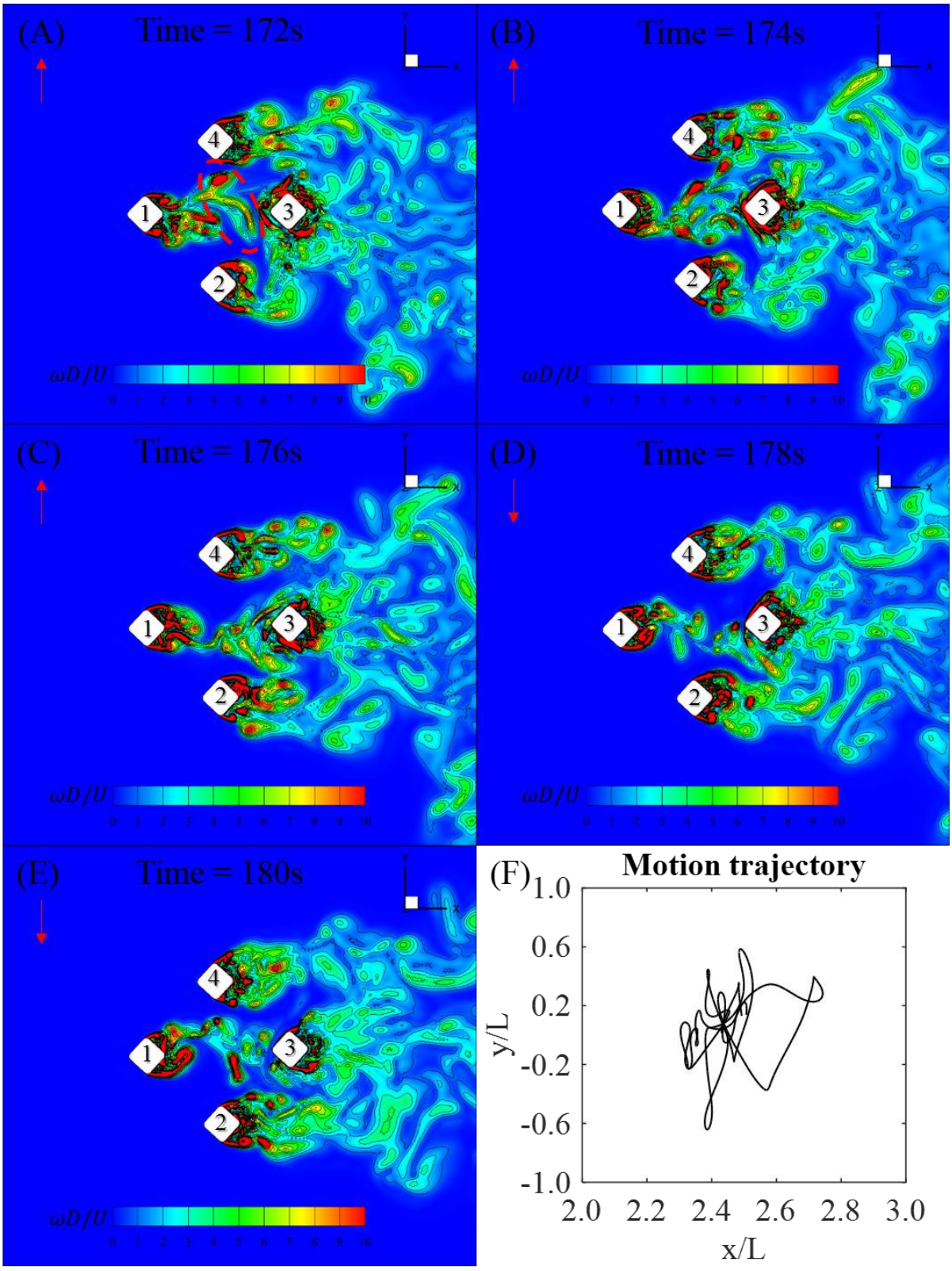

623

624 Fig. 40. A time series of the non-dimensional vorticity ($\omega D/U$) contours around the DDS at middle
625 draft showing the instantaneous flow fields around the DDS at Ur = 12.1 (A, B, C, D, E) and the non-
626 dimensional motion trajectory (F); the red arrow is the DDS transverse velocity direction.

When the reduced velocity reaches the “post lock-in” region, the vortices shed from the upstream column (Column 1) no longer impinge on the incidence flow faces of the portside and starboard side columns (Column 2 and 4). Instead, the vortices are seen to join the weak region of the portside and starboard side (see Fig. 37 to Fig. 40). The vortex street behind the Column 1, 2 and 4 can be clearly seen. In addition, it can be seen in Fig. 40(A) that parts of these vortices (red circled) do act on the incidence flow face of the downstream column (Column 3). As the vortices shed from the upstream column do not impinge on the portside and starboard side columns, the lift force coefficient and the transverse motion decrease and then remain a stable value in the measurement range of the “post lock-in” region in the present study.

4. Conclusions

This paper presented a numerical study on the forces and VIM of a deep-draft semi-submersible.

Two different models were considered, i.e., a stationary model and a VIM model. For the stationary model, the drag and lift force distributions on each structural member of the DDS are discussed and followed by the flow pattern analyses. The vortex interactions between each column are presented to explain the hysteresis phenomenon. The numerical model predicts forces well compared to the experimental results. For the VIM model, the motion and force on the whole structures are analysed, and the “pre lock-in”, “lock-in” and “post lock-in” phases can be accurately predicted in the present study. It is revealed that the discrepancies in the drag and lift forces between the numerical predictions and the experimental measurements at low reduced velocity is likely to be caused by the uncertainty in the experimental measurements at very low towing speed in the experiments. It is demonstrated that the numerical approach is a good way to predict the VIM responses at the low reduce velocity range.

Analysis of the drag and lift force coefficients on and the work done by different members of the DDS revealed that the portside and starboard side columns are the key structure members responsible for amplifying the VIM responses while the pontoons are acting to restrain VIM responses.

652 The present numerical study confirmed the hysteresis phenomenon - the peak lift force occurs slightly
653 earlier than the peak transverse motion. By examining the flow patterns at the time instantaneous near
654 the peak response, it is revealed that the hysteresis phenomenon between the force and motion is
655 mainly due to the vortices shed from the upstream column move back to impinge on one of the side
656 columns after impinging on the other side column and the symmetrical strong vortices which shed
657 from the side columns.

658 This study focuses on the 45 degree flow incidence on the DDS, more incidences should be
659 considered and examined in order to obtain a more generalized understanding on VIM of a multi-
660 column structures.

661 Acknowledgment

662 The authors would like to acknowledge the support of Newton Fund of Royal Academy of
663 Engineering UK (NRCP/1415/211) and the National Natural Science Foundation of China (Grant No.
664 51279104). This work made use of the facilities of N8 HPC Centre of Excellence, provided and
665 funded by the N8 consortium and EPSRC (Grant No. EP/K000225/1).

666 References

667 Antony, A., Vinayan, V., Halkyard, J., Kim, S.-J., Holmes, S., Spernjak, D., 2015. A CFD Based
668 Analysis of the Vortex Induced Motion of Deep-Draft Semisubmersibles, The Twenty-fifth
669 International Offshore and Polar Engineering Conference. International Society of Offshore
670 and Polar Engineers.
671 Antony, A., Vinayan, V., Madhavan, S., Parambath, A., Halkyard, J., Sterenborg, J., Holmes, S.,
672 Spernjak, D., Kim, S.J., Head, W., 2016. VIM Model Test of Deep Draft Semisubmersibles
673 Including Effects of Damping, Offshore Technology Conference. Offshore Technology
674 Conference.
675 CD-adapco, 2014. User Guide. Star-CCM+ Version 9.04.

676 Celik, I.B., Ghia, U., Roache, P.J., 2008. Procedure for estimation and reporting of uncertainty due to
677 discretization in CFD applications. Journal of fluids Engineering-Transactions of the ASME
678 130 (7).
679 Chen, J.M., Chiou, C.-C., 1997. Flow past a blunt flat plate subjected to the disturbance of incident
680 vortex street. Journal of Wind Engineering and Industrial Aerodynamics 66 (3), 179-196.
681 Fujarra, A.L.C., Rosetti, G.F., de Wilde, J., Gonçalves, R.T., 2012. State-of-art on vortex-induced
682 motion: a comprehensive survey after more than one decade of experimental investigation,
683 ASME 2012 31st International Conference on Ocean, Offshore and Arctic Engineering.
684 American Society of Mechanical Engineers, pp. 561-582.
685 Gonçalves, R.T., Fujarra, A.L.C., Rosetti, G.F., Kogishi, A.M., Koop, A., 2015. Effects of Column
686 Designs on the VIM Response of Deep-Draft Semi-Submersible Platforms, The Twenty-fifth
687 International Offshore and Polar Engineering Conference. International Society of Offshore
688 and Polar Engineers.
689 Gonçalves, R.T., Rosetti, G.F., Fujarra, A.L.C., Oliveira, A.C., 2012. Experimental study on vortex-
690 induced motions of a semi-submersible platform with four square columns, Part I: Effects of
691 current incidence angle and hull appendages. Ocean Engineering 54, 150-169.
692 Gonçalves, R.T., Rosetti, G.F., Fujarra, A.L.C., Oliveira, A.C., 2013. Experimental study on vortex-
693 induced motions of a semi-submersible platform with four square columns, Part II: Effects of
694 surface waves, external damping and draft condition. Ocean Engineering 62, 10-24.
695 Hong, Y., Choi, Y., Lee, J., Kim, Y., 2008. Vortex-induced motion of a deep-draft semi-submersible
696 in current and waves, The Eighteenth International Offshore and Polar Engineering
697 Conference. International Society of Offshore and Polar Engineers.
698 Kokkinis, T., Sandström, R.E., Jones, H.T., Thompson, H.M., Greiner, W.L., 2004. Development of a
699 Stepped Line Tensioning Solution for Mitigating VIM Effects in Loop Eddy Currents for the
700 Genesis Spar, ASME 2004 23rd International Conference on Offshore Mechanics and Arctic
701 Engineering. American Society of Mechanical Engineers, pp. 995-1004.

Koop, A., Rijken, O., Vaz, G., Maximiano, A., Rosetti, G., 2016. CFD Investigation on Scale and Damping Effects for Vortex Induced Motions of a Semi-Submersible Floater, Offshore Technology Conference. Offshore Technology Conference.

Lam, K., Li, J.Y., So, R.M.C., 2003b. Force coefficients and Strouhal numbers of four cylinders in cross flow. Journal of Fluids and structures 18 (3), 305-324.

Lee, S.-K., Chien, H.-P., Gu, H., 2014. CFD Study of Deep Draft SemiSubmersible VIM, Offshore Technology Conference-Asia. Offshore Technology Conference.

Lefevre, C., Constantinides, Y., Kim, J.W., Henneke, M., Gordon, R., Jang, H., Wu, G., 2013. Guidelines for CFD Simulations of Spar VIM, ASME 2013 32nd International Conference on Ocean, Offshore and Arctic Engineering. American Society of Mechanical Engineers, pp. V007T008A019-V007T008A019.

Liang, Y., Tao, L., Xiao, L., Liu, M., 2016. Experimental and Numerical Study on Vortex-Induced Motions of a Deep-Draft Semi-Submersible, Manuscript submitted for publication.

Liu, C.-H., Chen, J.M., 2002. Observations of hysteresis in flow around two square cylinders in a tandem arrangement. Journal of Wind Engineering and Industrial Aerodynamics 90 (9), 1019-1050.

Liu, M., Xiao, L., Lyu, H., Tao, L., 2015. Numerical Analysis of Pontoon Effect on Flow-Induced Forces of the Deep Draft Semisubmersible in a Cross-Flow, ASME 2015 34th International Conference on Ocean, Offshore and Arctic Engineering. American Society of Mechanical Engineers, pp. V001T001A030-V001T001A030.

Ljungkrona, L., Norberg, C.H., Sunden, B., 1991. Free-stream turbulence and tube spacing effects on surface pressure fluctuations for two tubes in an in-line arrangement. Journal of Fluids and structures 5 (6), 701-727.

Ma, W., Wu, G., Thompson, H., Prislin, I., Maroju, S., 2013. Vortex induced motions of a column stabilized floater, Proceedings of the DOT International Conference, pp. 22-24.

Magee, A., Sheikh, R., Guan, K.Y.H., Choo, J.T.H., Malik, A.M.A., Ghani, M.P.A., Abyn, H., 2011. Model tests for VIM of multi-column floating platforms, ASME 2011 30th International

729 Conference on Ocean, Offshore and Arctic Engineering. American Society of Mechanical
730 Engineers, pp. 127-136.
731 Rijken, O., Leverette, S., 2008. Experimental Study into Vortex Induced Motion Response of Semi
732 Submersibles with Square Columns, ASME 2008 27th International Conference on Offshore
733 Mechanics and Arctic Engineering. American Society of Mechanical Engineers, pp. 263-276.
734 Rijken, O., Leverette, S., 2009. Field measurements of vortex induced motions of a deep draft
735 semisubmersible, ASME 2009 28th International Conference on Ocean, Offshore and Arctic
736 Engineering. American Society of Mechanical Engineers, pp. 739-746.
737 Rijken, O., Schuurmans, S., Leverette, S., 2011. Experimental investigations into the influences of
738 SCRs and appurtenances on DeepDraft Semisubmersible Vortex Induced Motion response,
739 Proceedings of the 30th International Conference on Ocean, Offshore and Arctic Engineering,
740 Rotterdam, The Netherlands, OMAE2011-49365.
741 Sarpkaya, T., 2004. A critical review of the intrinsic nature of vortex-induced vibrations. Journal of
742 Fluids and structures 19 (4), 389-447.
743 Schewe, G., 1983. On the force fluctuations acting on a circular cylinder in crossflow from subcritical
744 up to transcritical Reynolds numbers. Journal of Fluid Mechanics 133, 265-285.
745 Shur, M.L., Spalart, P.R., Strelets, M.K., Travin, A.K., 2008. A hybrid RANS-LES approach with
746 delayed-DES and wall-modelled LES capabilities. International Journal of Heat and Fluid
747 Flow 29 (6), 1638-1649.
748 Spalart, P.R., Jou, W.H., Strelets, M., Allmaras, S.R., 1997. Comments on the feasibility of LES for
749 wings, and on a hybrid RANS/LES approach. Advances in DNS/LES 1, 4-8.
750 Tan, J.H.C., Magee, A., Kim, J.W., Teng, Y.J., Zukni, N.A., 2013. CFD Simulation for Vortex
751 Induced Motions of a Multi-Column Floating Platform, ASME 2013 32nd International
752 Conference on Ocean, Offshore and Arctic Engineering. American Society of Mechanical
753 Engineers, pp. V007T008A066-V007T008A066.
754 Vikestad, K., Vandiver, J.K., Larsen, C.M., 2000. Added mass and oscillation frequency for a circular
755 cylinder subjected to vortex-induced vibrations and external disturbance. Journal of Fluids
756 and structures 14 (7), 1071-1088.

Vinayan, V., Antony, A., Halkyard, J., Kim, S.-J., Holmes, S., Spernjak, D., 2015. Vortex-Induced Motion of Deep-Draft Semisubmersibles: A CFD-Based Parametric Study, ASME 2015 34th International Conference on Ocean, Offshore and Arctic Engineering. American Society of Mechanical Engineers, pp. V002T008A003-V002T008A003.

Waals, O.J., Phadke, A.C., Bultema, S., 2007. Flow Induced Motions on Multi Column Floaters, ASME 2007 26th International Conference on Offshore Mechanics and Arctic Engineering. American Society of Mechanical Engineers, pp. 669-678.

Zhang, H., Yang, J., Xiao, L., Lu, H., 2014. Study on added mass coefficient and oscillation frequency for a Truss Spar subjected to Vortex-Induced Motions. Ships and Offshore Structures 9 (1), 54-63.

List of Tables

List of Figures

799 Fig. 12. Mean lift coefficient ($\overline{C}_L$) on each member of the stationary DDS.

800 Fig. 13. Lift force coefficient time history on different members of the DDS at $Re = 4.3 \times 10^4$,
801 including locally zoomed in the last 6s.

802 Fig. 14. A time series of the pressure distribution around the DDS at middle draft showing the
803 instantaneous flow fields around the DDS at $Re = 4.3 \times 10^4$ corresponding to the lift force coefficient
804 time history (A: 120.6s; B: 122.4s; C: 124.2s; D: 126.0s).

805 Fig. 15. A time series of non-dimensional spanwise vorticity ($\vec{\omega}_z D/U$) contours around the DDS at the
806 middle draft level showing the instantaneous flow fields around the DDS at $Re = 4.3 \times 10^4$
807 corresponding to the lift force coefficient time history (A: 120.6s; B: 122.4s; C: 124.2s; D: 126.0s).

808 Fig. 16. Non-dimensional transverse characteristic amplitudes (A_y/L), the *Ur* is defined based on the
809 natural period of the transverse motion.

810 Fig. 17. Non-dimensional in-line characteristic amplitudes (A_x/L), the *Ur* is defined based on the
811 natural period of the transverse motion.

812 Fig. 18. Non-dimensional yaw characteristic amplitudes, the *Ur* is defined based on the natural period
813 of the yaw motion.

814 Fig. 19. Mean drag coefficient ($\overline{C}_D$) from the numerical and experimental results on the VIM model,
815 the *Ur* is defined based on the natural period of the transverse motion.

816 Fig. 20. Root mean square lift coefficient (C_{Lrms}) from the numerical and experimental results on the
817 VIM model, the *Ur* is defined based on the natural period of the transverse motion.

818 Fig. 21. Added mass coefficient (C_a) of the VIM model from the numerical predictions and the
819 experiments, the *Ur* is defined based on the natural period of the transverse motion.

820 Fig. 22. FFT of the transverse motions and the lift force coefficients at Ur = 3.9, (a) transverse
821 motion; (b) lift force coefficient.

822 Fig. 23. FFT of the transverse motions and the lift force coefficients at Ur = 5.1, (a) transverse
823 motion; (b) lift force coefficient.

824 Fig. 24. FFT of the transverse motions and the lift force coefficients at Ur = 6.6, (a) transverse
825 motion; (b) lift force coefficient.

826 Fig. 25. FFT of the transverse motions and the lift force coefficients at Ur = 8.9, (a) transverse
827 motion; (b) lift force coefficient.

828 Fig. 26. FFT of the transverse motions and the lift force coefficients at Ur = 12.1, (a) transverse
829 motion; (b) lift force coefficient.

830 Fig. 27. Mean drag coefficients ($\overline{C}_D$) on each member of the DDS from the VIM model.

831 Fig. 28. Root mean square lift coefficients (C_{Lrms}) on each member of the DDS from the VIM model.

832 Fig. 29. Work done by each member of the DDS on VIM model.

833 Fig. 30. Definition of the regions around the individual column.

834 Fig. 31. A time series of the non-dimensional spanwise vorticity ($\overrightarrow{\omega}_z D/U$) contours around the DDS at
835 middle draft showing the instantaneous flow fields around the DDS at Ur = 3.9 (A, B, C, D, E) and
836 the non-dimensional transverse motion (y/L) time history (F); the red arrow is the DDS transverse
837 velocity direction.

838 Fig. 32. A time series of the non-dimensional vorticity ($\omega D/U$) contours around the DDS at middle
839 draft showing the instantaneous flow fields around the DDS at Ur = 3.9 (A, B, C, D, E) and the non-
840 dimensional motion trajectory (F); the red arrow is the DDS transverse velocity direction.

841 Fig. 33. A time series of the non-dimensional spanwise vorticity ($\vec{\omega}_z D/U$) contours around the DDS at
842 middle draft showing the instantaneous flow fields around the DDS at Ur = 5.1 (A, B, C, D, E) and
843 the non-dimensional transverse motion (y/L) time history(F); the red arrow is the DDS transverse
844 velocity direction.

845 Fig. 34. A time series of the non-dimensional vorticity ($\omega D/U$) contours around the DDS at middle
846 draft showing the instantaneous flow fields around the DDS at Ur = 5.1 (A, B, C, D, E) and the non-
847 dimensional motion trajectory (F); the red arrow is the DDS transverse velocity direction.

848 Fig. 35. A time series of the non-dimensional spanwise vorticity ($\vec{\omega}_z D/U$) contours around the DDS at
849 middle draft showing the instantaneous flow fields around the DDS at Ur = 6.6 (A, B, C, D, E) and
850 the non-dimensional transverse motion (y/L) time history (F); the red arrow is the DDS transverse
851 velocity direction.

852 Fig. 36. A time series of the non-dimensional vorticity ($\omega D/U$) contours around the DDS at middle
853 draft showing the instantaneous flow fields around the DDS at Ur = 6.6 (A, B, C, D, E) and the non-
854 dimensional motion trajectory (F); the red arrow is the DDS transverse velocity direction.

855 Fig. 37. A time series of the non-dimensional spanwise vorticity ($\vec{\omega}_z D/U$) contours around the DDS at
856 middle draft showing the instantaneous flow fields around the DDS at Ur = 8.9 (A, B, C, D, E) and
857 the non-dimensional transverse motion (y/L) time history (F); the red arrow is the DDS transverse
858 velocity direction.

Fig. 38. A time series of the non-dimensional vorticity ($\omega D/U$) contours around the DDS at middle draft showing the instantaneous flow fields around the DDS at Ur = 8.9 (A, B, C, D, E) and the non-dimensional motion trajectory (F); the red arrow is the DDS transverse velocity direction.

Fig. 39. A time series of the non-dimensional spanwise vorticity ($\vec{\omega}_z D/U$) contours around the DDS at middle draft showing the instantaneous flow fields around the DDS at Ur = 12.1 (A, B, C, D, E) and the non-dimensional transverse motion (y/L) time history (F); the red arrow is the DDS transverse velocity direction.

Fig. 40. A time series of the non-dimensional vorticity ($\omega D/U$) contours around the DDS at middle draft showing the instantaneous flow fields around the DDS at Ur = 12.1 (A, B, C, D, E) and the non-dimensional motion trajectory (F); the red arrow is the DDS transverse velocity direction.